

---

## Geochemical evidence of mantle reservoir evolution during progressive rifting along the western Afar margin

Tyrone O. Rooney<sup>a,\*</sup>, Paul Mohr<sup>b</sup>, Laure Dosso<sup>c</sup>, Chris Hall<sup>d</sup>

<sup>a</sup> Dept. of Geological Sciences, Michigan State University, East Lansing, MI 48824, USA

<sup>b</sup> Tonagharrun, Corrandulla, Co. Galway, Ireland

<sup>c</sup> Laboratoire Domaines Océaniques, UMR 6538, CNRS, Ifremer, 29280 – Plouzané, France

<sup>d</sup> Dept. of Earth and Environmental Sciences, University of Michigan, Ann Arbor, MI 48109, USA

\*: Corresponding author : Tyrone O. Rooney, Tel.: +1 517 432 5522 ; email address : [rooneyt@msu.edu](mailto:rooneyt@msu.edu)

---

### Abstract:

The Afar triple junction, where the Red Sea, Gulf of Aden and African Rift System extension zones converge, is a pivotal domain for the study of continental-to-oceanic rift evolution. The western margin of Afar forms the southernmost sector of the western margin of the Red Sea rift where that margin enters the Ethiopian flood basalt province. Tectonism and volcanism at the triple junction had commenced by ~31 Ma with crustal fissuring, diking and voluminous eruption of the Ethiopian-Yemen flood basalt pile. The dikes which fed the Oligocene-Quaternary lava sequence covering the western Afar rift margin provide an opportunity to probe the geochemical reservoirs associated with the evolution of a still active continental margin. <sup>40</sup>Ar/<sup>39</sup>Ar geochronology reveals that the western Afar margin dikes span the entire history of rift evolution from the initial Oligocene flood basalt event to the development of focused zones of intrusion in rift marginal basins. Major element, trace element and isotopic (Sr-Nd-Pb-Hf) data demonstrate temporal geochemical heterogeneities resulting from variable contributions from the Afar plume, depleted asthenospheric mantle, and African lithosphere. The various dikes erupted between 31 Ma and 22 Ma all share isotopic signatures attesting to a contribution from the Afar plume, indicating this initial period in the evolution of the Afar margin was one of magma-assisted weakening of the lithosphere. From 22 Ma to 12 Ma, however, diffuse diking during continued evolution of the rift margin facilitated ascent of magmas in which depleted mantle and lithospheric sources predominated, though contributions from the Afar plume persisted. After 10 Ma, magmatic intrusion migrated eastwards towards the Afar rift floor, with an increasing fraction of the magmas derived from depleted mantle with less of a lithospheric signature. The dikes of the western Afar margin reveal that magma generation processes during the evolution of this continental rift margin are increasingly dominated by shallow decompressional melting of the ambient asthenosphere, the composition of which may in part be controlled by preferential channeling of plume material along the developing neo-oceanic axes of extension.

### 1. Introduction

---

Early quantitative tectonic models explained the generation of mantle melt in extensional zones in terms of simple adiabatic decompression of the asthenosphere (e.g., White and McKenzie, 1989). However, the stresses required to rupture typical continental lithosphere may not be available from plate tectonic processes alone, and hybrid models were subsequently developed in

45 which magma provides additional impetus for lithospheric rifting (e.g., Buck, 2004; Buck, 2006;  
46 Bialas et al., 2010). Lateral variations in lithospheric thickness and rheology may also localize  
47 strain and magmatism during rifting (e.g., Ebinger and Sleep, 1998; van Wijk et al., 2008).  
48 Upwelling, buoyant asthenosphere contributes to plate driving forces, and may generate  
49 significant volumes of melt across a broad region (e.g., Huisman et al., 2001). The presence of  
50 buoyant melt can facilitate the intrusion of dikes into thick continental lithosphere at  
51 comparatively small extensional stresses, and this heating can significantly reduce the strength of  
52 the plate, further facilitating extension (e.g., Fialko and Rubin, 1999; Buck, 2004; Bialas et al.,  
53 2010). Thus, the initial phase of rifting above a mantle plume may be marked by a pulse of  
54 widespread dike intrusion (e.g., Renne et al., 1996; Fialko and Rubin, 1999; Klausen and Larsen,  
55 2002). During the later stages of continental rifting, extension occurs principally by dike  
56 intrusion into a thinned lithosphere (Ebinger and Casey, 2001; Keranen et al., 2004; Rooney et  
57 al., 2005; Daly et al., 2008; Keir et al., 2009; Bastow et al., 2010; Ebinger et al., 2010; Wright et  
58 al., 2012), before a final stage of plate stretching and associated decompression melting  
59 characterizing the final stages of continent-ocean transition (e.g., Bastow and Keir, 2011). Key  
60 unresolved questions remain concerning the geochemical signature(s) of the melt sources during  
61 the initial stages of continental rifting, and the evolution of these sources as rifting continues.

62 The mafic lavas and dikes of continental rift margins provide a window on the evolution of  
63 the underlying mantle sources that have contributed to a developing rift. Unfortunately, most  
64 rifted margins are now at least partly submarine and relatively inaccessible. However, sustained  
65 uplift above an active mantle plume in Ethiopia has provided a sub-aerial instance of a  
66 continental rift margin in the final stages of its evolution. Observations around the Afar triple-rift  
67 junction confirm that magmatic intrusion and crustal heating have played a significant role in

68 facilitating lithospheric extension and rupture (Berckhemer et al., 1975; Mohr, 1983a; Buck,  
69 2004; Buck, 2006; Bialas et al., 2010; Bastow and Keir, 2011). The western margin of Afar  
70 provides an excellent site for probing the space-time relationships between magmatism and  
71 extension across a rift margin (e.g., Keir et al., 2011b). In this paper we examine the  
72 geochemical, structural, and geochronological properties of the dikes that intrude this continental  
73 margin, and explore the participation of the various mantle and lithospheric geochemical  
74 reservoirs that contribute to the evolution of this margin.

75

## 76 **2. The Western Afar Rift Margin**

### 77 2.1 Setting and Form

78 The well-studied western Afar margin separates the stable and relatively undeformed  
79 post-basement cover of the Ethiopian Plateau to the west from the Cenozoic and presently active  
80 extensional faulting, fissuring, and magmatism of the Afar depression (Gortani and Bianchi,  
81 1937; Abbate et al., 1968; Abbate and Sagri, 1969; Mohr, 1971; Megrue et al., 1972; Gortani and  
82 Bianchi, 1973; Justin-Visentin and Zanettin, 1974; Mohr, 1983a; Hart et al., 1989; Wolfenden et  
83 al., 2005). The 800-km long western Afar margin runs in a gently curvilinear plan from Asmara  
84 in the north to Addis Ababa in the south, with the exception of a large dextral offset at latitude  
85 13°N (Fig. 1). This coincides with the northern limit of the thick flood-lava sequence on the  
86 plateau, and also marks a structural contrast: to the north, seismically active stepped normal  
87 faults downthrown towards the rift are concentrated within a narrower margin (40 km); to the  
88 south, antithetically faulted flood-basalts cap a wider (80 km) monoclinical margin (Mohr, 1962;  
89 Abbate and Sagri, 1969; Ayele et al., 2007; Keir et al., 2011a). This southern sector of the  
90 margin can in turn be divided into two sub-sectors to either side of a proposed accommodation

91 zone (Wolfenden et al., 2005). North of latitude 11°N, the flood-basalt pile comprises 31-29 Ma  
92 lavas and tuffs locally overlain by a cover of ~25-22 Ma flows (Justin-Visentin and Zanettin,  
93 1974; Kieffer et al., 2004). Proceeding south from 11°N to Addis Ababa, the Oligocene flood-  
94 basalt pile is capped by progressively younger lavas that include a volumetrically significant  
95 proportion of silicic members (Zanettin, 1992; Ukstins et al., 2002). The margin transect chosen  
96 for this study is located immediately north of the chronological divide at 11°N (Fig. 1), taking  
97 advantage of the Desse-Eloa highway (Mohr, 1971; Gortani and Bianchi, 1973).

98

## 99 2.2. Regional Stratigraphy

100 Expanding upon earlier studies detailing the stratigraphic and structural characteristics of  
101 the western Afar margin (Abbate et al., 1968; Gortani and Bianchi, 1973; Justin-Visentin and  
102 Zanettin, 1974; Mohr, 1983b), a new stratigraphy for the entire southern sector of the western  
103 Afar margin has been compiled by Wolfenden et al., (2005). It comprises four magmatic  
104 episodes (Table 1) which relate to a sequential, riftward production of three elongate rift-parallel  
105 volcanic basins imposed on the regional Oligocene flood-basalt pile:

106 The „Stage 1 Basin“ developed at the western end of the transect, contemporaneous with  
107 eruption of basalts and agglomerates derived from the 25-22 Ma-old Gugufu shield volcano  
108 located on the plateau rim (Kieffer et al., 2004). These Dese Formation lava flows are rarely  
109 more than a few meters thick, and lie with local unconformity on the lateritized and strongly  
110 zeolitised Oligocene pile. Characteristic lithologies are megacrystic plagioclase basalt, aphyric  
111 basalt, and subordinate olivine- and olivine-augite-phyric basalt. The pyroclastic members  
112 include fine basaltic tuff (in one instance carrying blocks of underlying, unexposed Jurassic  
113 limestone) and massive agglomerate proximate to basalt pipe vents. Silicic ash-fall and ash-flow

114 tuff beds are restricted to the topmost part of the Dese Formation. The „Stage 2 Basin“ is situated  
115 near the median of the Dese-Eloa transect. Its fill of flood basalts and intercalated ignimbrites  
116 compose the early-mid Miocene Burka Formation (Wolfenden et al., 2005), again lying with  
117 unconformity on the Oligocene stratoid pile. The „Stage 3 Basin“ at the eastern end of the  
118 transect contains the late Miocene-Pliocene Dahla Series basalts, previously termed Fursa  
119 Basalts (Justin-Visentin and Zanettin, 1974).

120

### 121 2.3. Dikes and faults of the Dese – Eloa transect

122 Antithetic faulting parallel to the NNW regional strike of the margin has produced tilted  
123 crustal blocks typically 10-20 km across (Abbate and Sagri, 1969; Mohr, 1983b). The resultant  
124 dips of the Oligocene stratoid pile average 20°-30° in the west sector of the transect, 15°-30° in  
125 the central sector, and 15°-20° in the east (Table 2). However, occasional deep gorge exposures  
126 reveal maximum dips of 30° in the west and 45° in the east, indicative of second-generation  
127 block faulting (Morton and Black, 1975). Fault-plane dip is directed overwhelmingly westward,  
128 and averages 80° in the western sector. Common 70° dips in the central and eastern sectors are  
129 interspersed with local 35°-45° dips. The predominating margin-parallel faults can number up to  
130 forty within a kilometre-wide zone, the largest with measured throws in excess of one hundred  
131 metres, the majority with west-side downthrows. Subordinate faults oblique to the regional trend  
132 include N-dipping ENE faults (yielding a southerly component of dip to the stratoid pile), S-  
133 dipping WNW faults, and W-dipping NNE faults (Mohr, 1971). Striations on some fault planes  
134 prove a component of lateral slip. Small sinusoidal folds with ENE-trending axes are pervasive  
135 in some areas.

136 Nearly 80 percent of all dikes strike parallel or near-parallel to the dominant NNW-  
137 trending faults that define the margin. The oblique strikes of a minority of dikes are mirrored by  
138 subordinate fault trends (Table 2). However, while dikes and faults share common conjugate  
139 trends within the western Afar margin (Abbate and Sagri, 1969; Mohr, 1971; Justin-Visentin and  
140 Zanettin, 1974; Mohr, 1983b), the major zones of fissuring and fracturing are separate and rarely  
141 overlap. The tendency to spatial segregation of fault zones and dike swarms in the western Afar  
142 margin may owe not only to temporal separation of the two processes in an evolving stress field,  
143 but also to the role, as yet not fully evaluated, of magmatic centres from which dikes were  
144 laterally propagated. The longest *exposed* dike identified in the transect is almost one kilometre,  
145 but a consideration of dikes elsewhere in Ethiopia makes it likely that some may extend for at  
146 least 10 km (Mohr, 1999; Schultz et al., 2008). The median dike width over the entire Desse-  
147 Eloa transect is 1.5 m, with a mean of 3.5 m (Mohr, 1971, 1983b).

148 Dike distribution across the Desse-Eloa transect is irregular (Mohr, 1971, Fig. 1), in part  
149 influenced by local volcanic centres to north and south. At the western plateau end of the  
150 transect, between Desse (2525 m) and Combolcha (1875 m), a pattern of Oligo-Miocene  
151 antithetic faulting trending N-NNW (now largely masked under Miocene Gugufu volcanics)  
152 has been superposed with complex Quaternary marginal graben faulting (Mohr, 1962). Near  
153 Dessie, Oligo-Miocene fault-blocks are tilted 10-30° (rarely as steeply as 45°) directed between  
154 E and NE, whereas near Combolcia tilts of 20-30° are directed between E and SE. The dikes  
155 exposed in this sector relate almost wholly to the covering Gugufu volcanic sequence, and trend  
156 N-S, slightly oblique to the NNW-SSE regional structural trend. Dike dips range between 60°  
157 and vertical, directed west as for the major faults (Mohr, 1971; Mohr, 1983b). Subordinate dikes  
158 trending ENE persist further eastward into the central sector of the transect.

159           The descent east from Combolcha and the Ancharo rim of the Borkenna graben (Fig. 1)  
160 reaches a NNW-SSE zone of intense faulting in the Chaleka valley (1520 m) (Abbate & Sagri,  
161 1969). Through this sector of the traverse, riftward-tilted blocks of lateritized, zeolitized  
162 Oligocene flood-basalts locally manifest small sinusoidal folds also found in the Desse-  
163 Combolcia sector. Feeder dikes for the lavas are mostly in 3-D parallelism with the regional  
164 NNW-trending faults, and strike towards the Ardibbo volcanic centre, 40 km to the north. Large  
165 (< 35 m-wide) feeder pipes also occur, ringed with precursor, intensely baked agglomerate.  
166 Subordinate dikes of ESE trend (SW dip) and NNE trend (W dip) can form a symmetrical  
167 complementary pair about the dominant NNW dikes. If synchronous, they indicate a maximum  
168 principal horizontal stress directed along the strike of the margin (Mohr, 1971), concurring with  
169 the geometry of the folds and some small reversed faults in the flood-basalt pile.

170           From the Chaleka valley east up to the Batie saddle (1670 m), interspersed NNW and  
171 NNE-trending dikes expose no cross-cutting relationships. Some NNW dikes became normal slip  
172 planes during solidification, but others were subject to later oblique, brittle displacement. For  
173 example, intrusion EKA-119, a 6 m-wide, near-vertical N300° dike was displaced by a N030°  
174 fault dipping 75° SE, the 3-D orientation of neighbouring NNE dikes.

175           Down the eastern slope of the Batie saddle, the transect declines rapidly to Wadi Burca  
176 (1000 m), then more gently onto the Enelu plain (950 m). From the eastern side of the plain  
177 (Wadi Fursa), the decline resumes to Eloa (675 m) at the western edge of the Afar floor (Fig. 1).  
178 Between 4 and 8 km east of Batie, both dikes and faults are numerous and share a NNE trend  
179 distinctly oblique to the regional margin trend. The maximum measured dilatation for the entire  
180 Desse-Eloa transect occurs here: a total dike width of 60 m opened within a 1 km-wide crustal  
181 strip, indicating 6% extension. East from this swarm for 15 km, limited exposures of tilted

182 Oligocene flood-basalts in the Burca valley („Stage 2 Basin“ of Wolfenden et al., 2005) reveal  
183 rare thin, fractured dikes, until more typical dikes resume in the Fursa valley („Stage 3 Basin“ of  
184 Wolfenden et al., 2005).

185

### 186 **3. Analytical Techniques**

187 Dikes in preference to lavas have been selected for this study, as they form in response to both  
188 the structural and magmatic evolution of the margin. Furthermore, flood basalt lavas can flow  
189 significant distances from their vents, thus potentially skewing spatial studies.

#### 190 3.1 Geochronology

191 Ten representative samples that did not exhibit any indications of alteration were selected  
192 for  $^{40}\text{Ar}$ - $^{39}\text{Ar}$  step heating analysis at the Argon Geochronology Laboratory at the University of  
193 Michigan. Fresh matrix chips (0.2g) were carefully handpicked under a binocular microscope  
194 and Ar analysis was undertaken using standard procedures outlined in Frey et al., (2007).

195 Samples were wrapped in pure Al foil packets and irradiated in location 5C of the McMaster  
196 Nuclear Reactor. Samples were step-heated using a continuous 5W Ar-ion laser and Ar isotopes  
197 were analyzed using a VG-1200S mass spectrometer operating with a total electron emission  
198 setting of 150 micro-amps (see Table 3 and supplemental table for further analytical  
199 information).

200

#### 201 3.2 Major and Trace elements.

202 Thirty-five samples (1-2 kg) were taken from the least-altered dikes, and for each dike  
203 from a position intermediate between the centre and margin. They were subsequently trimmed to  
204 exclude visible alteration/weathering. Sample billets were polished to remove saw marks and



205 cleaned in an ultra sonic bath with deionised water. After drying, the billets were crushed in a  
206 steel jaw-crusher and then powdered in a ceramic Bico flat plate grinder. The sample powders  
207 were fused into lithium tetraborate glass disks using the procedures outlined in Deering et al.,  
208 (2008). Major elements, Zr, Sr, Rb and Ni were analyzed by Bruker XRF, the balance of the  
209 trace elements were obtained by laser-ablation using a Cetac LSX-200 coupled to a Micromass  
210 Platform ICP-MS at Michigan State University. Trace element reproducibility based on standard  
211 analyses (see supplemental data) is typically better than 5% (Vogel et al., 2006).

212

### 213 3.3 Isotope Geochemistry

214 Twelve representative samples of the western Afar dikes were chosen for radiogenic  
215 isotope analysis at the Laboratoire Domaines Océaniques of CNRS/ Ifremer, France. Samples  
216 were chosen on the basis of a) representing all dike groups, and b) selecting the most primitive  
217 magmas possible. Powdered samples (300 to 600 mg) were dissolved in Savillex beakers using  
218 ultrapure concentrated HF-HBr (3:1 in volume). Separation and analyses of Pb, Hf, Sr and Nd  
219 were performed from the same sample dissolution using 4 different columns.

220 Column 1 : to minimize Pb blanks, Pb separation was performed first, using the standard  
221 anion exchange method in an HBr medium (Tilton, 1973; Manhès et al., 1978). After loading the  
222 sample, the Pb column was washed with 0.5 M HBr. The fraction passing through the column  
223 directly following loading and subsequent washing was collected and evaporated in 6 M HCl for  
224 further separation of Hf-Sr-Nd on column 2. We repeated the anion exchange method a second  
225 time to purify the Pb fraction which was collected in 6 M HCl.

226 Column 2 : the Hf-Sr-Nd fraction was taken up in 0.5 M HCl/0.15 M HF and loaded on a  
227 cation column (microcolumn Savillex, 30 ml, 6.4 mm ID x 9.6 mm OD x 25 cm). The Hf-Ti

228 fraction was eluted in the first 6 ml with 0.5 M HCl/0.15 M HF. 22 ml of 3M HCl was then  
229 added to the column to wash for Fe and Rb, and the Sr fraction was then collected in 6 ml and  
230 evaporated to dryness. 8 ml of 4M HNO<sub>3</sub> was then added to the same column to separate Ba from  
231 the rare earth elements, which were then recovered in a 6 ml fraction.

232 Column 3 : following evaporation, the rare earth fraction was placed on a Biorad Econo-  
233 Col Polyprop 0.8 cm x 4 cm loaded with Eichrom LN resin. Nd was separated from Ce and Sm  
234 using 13 ml of 0.2 M HCl and eluted using 4 ml of 0.35 M HCl.

235 Column 4 : the Hf-Ti fraction separated using column 2 is evaporated and taken up in 6  
236 M HCl containing a trace of H<sub>2</sub>O<sub>2</sub>. The Hf-Ti separation was performed using a 5 ml pipette tip  
237 loaded with 100 mg of Eichrom LN resin that was washed with 6 M HCl. 10 ml 6 M HCl with  
238 50 µl of H<sub>2</sub>O<sub>2</sub> were used to elute Ti. Hf was subsequently collected in 5 ml of 2 M HF.

239 Pb, Nd, and Hf were analyzed by MC-ICPMS on the Thermo Neptune at Ifremer. Sr was  
240 analyzed by TIMS using the Finnigan MAT-26X also located at Ifremer. Standards, blanks and  
241 analytical errors are given in the caption to Table 4.

242

## 243 **4. Results and classification of dikes**

### 244 4.1 Geochronology

#### 245 4.1.1 *Cross-cutting relationships*

246 Pervasive zeolitisation of the Oligocene stratoid lavas, and to a lesser extent their feeder  
247 dikes, was accomplished before intrusion of the 25-22 Ma-old Gugufu dikes, consistent with  
248 the expected thermal history of a 1 km-thick lava pile (Walker, 1960; Jepsen and Athearn, 1962).  
249 The essentially perpendicular relationship of the flood basalt lavas to the great majority of dikes  
250 indicates that ratchet faulting and block tilting of the lava pile occurred after fissuring and

251 magmatic injection was largely accomplished. Nevertheless, in some cases the time interval  
252 between fissuring faulting was brief, as evidenced by ductile deformation along dike axes.  
253 Young intra-margin faulting is exemplified in a 12 Ma-old dike (EKA-119 on the Batié saddle)  
254 displaced by a NNE-trending fault. In general, however, field studies across the western Afar  
255 margin are not yet sufficient to distinguish the relative age-relationships among the several  
256 trends of dikes and faults.

#### 257 4.1.2 $^{40}\text{Ar}/^{39}\text{Ar}$ dating

258 The results of the  $^{40}\text{Ar}/^{39}\text{Ar}$  analyses are shown in Table 3. Replicate analyses were  
259 performed for each sample and a series of  $^{40}\text{Ar}/^{39}\text{Ar}$  model ages were calculated. Sample EAD-  
260 111 yielded plateau ages for both of the analyses that were performed, but there were also signs  
261 of a “saddle” shape to the age spectrum, suggesting a small quantity of excess  $^{40}\text{Ar}$ . The  
262 combined isochron age (CIA) is based on a true isochron through all 26 gas fractions with a  
263 slightly elevated initial  $^{40}\text{Ar}/^{36}\text{Ar}$  ratio of 298.5. Although the CIA is not significantly different  
264 from the average of the error weighted plateau age (EWP) values, we consider the CIA to be the  
265 preferred age (23.57 Ma) for this sample, because the EWP values may be slightly biased to an  
266 erroneously high age.

267 For sample EAD-114, there are no EWP segments and there are definite signs of  $^{40}\text{Ar}$   
268 loss in the lowest temperature fractions. In addition, there is a monotonic decrease in apparent  
269 ages with increasing release temperatures, which suggests that there was internal redistribution  
270 of  $^{39}\text{Ar}$  due to recoil. Therefore, we regard the average of the reduced integrated ages (RIA) ages  
271 to be the preferred age for this unit (24.76 Ma). In contrast, sample EKA-112B has EWP values  
272 over the entire age spectrum for both replicates. All four model ages agree within error and given

273 that there is no sign of significant Ar loss or artifacts due to recoil, the average EWP value is our  
274 preferred age for this sample (30.77 Ma).

275 Three replicate analyses were performed for sample EKA-116 and the age spectra show  
276 definite signs of Ar loss in the low temperature fractions, probably due to alteration minerals.  
277 Nonetheless, all three samples had EWP segments, indicating relatively good Ar retention for the  
278 higher temperature gas fractions. However, there is a nearly monotonic decline in ages with  
279 increasing release temperatures, suggesting the possibility for recoil artifacts. Therefore, we  
280 prefer the average of RIA (29.78 Ma), which avoids the Ar-loss portions of the age spectra, but  
281 correctly accounts for the possibility of internal redistribution of  $^{39}\text{Ar}$  from recoil.

282 Sample EKA-119 also had three replicate analyses and all of the runs had EWP  
283 segments. However, there are definite signs of a “saddle” shape, which suggests the possibility  
284 of excess  $^{40}\text{Ar}$ . In order to minimize the possibility of having a bias to high ages, we prefer the  
285 CIA age through 37 gas fractions, which yields an “errorchron” with an initial  $^{40}\text{Ar}/^{36}\text{Ar}$  value of  
286 297.7 and an age that is only slightly older than the average EWP age (12.51 Ma). For sample  
287 EKA-120, only two of the three analyses yielded EWP segments and because of significant  
288 apparent age variations that correspond with changes in the Ca/K ratio, we regard the average  
289 RIA age to be the most reliable age estimate (27.37 Ma).

290 Sample EKA-140A exhibited rather poor reproducibility and only one of the two  
291 analyses gave an EWP segment. The age of this sample is not well constrained, but we consider  
292 that the average RIA value is the best estimate for the age of this unit (8.31 Ma). For sample  
293 EKA-153, there are signs of significant Ar loss in the low temperature gas fractions and given  
294 that there are no plateau segments, the RIA average is likely to be the best date for this sample  
295 (20.55 Ma).

296 Table 3 also shows K-Ar ages derived from the data in Megrue et al. (1972), with ages  
297 being updated to the decay and K composition constants in Steiger and Jäger (1977) and error  
298 estimates based upon the listed error estimates for K and  $^{40}\text{Ar}^*$ . For samples EAD-111 and EAD-  
299 114, there is very good concordance between our Ar-Ar ages and the K-Ar ages in Megrue et al.  
300 (1972). For all of the other samples, the K-Ar ages are systematically higher than the Ar-Ar ages,  
301 although in most cases, this difference is only slightly larger than the error estimate in the K-Ar  
302 age. It is possible that the K-Ar ages are biased high because of the presence of excess Ar, a  
303 common problem with dike samples. Even though some host rock samples in Megrue et al.,  
304 (1972) show ages that are greater than the dike ages, Hyodo and York (1993) showed that it is  
305 possible for an excess Ar “wave” to propagate from a dike and contaminate hosting rock. Care  
306 must be taken when interpreting K-Ar data that does not have the detail that is shown in Ar-Ar  
307 age spectra. Sample EKA-140A gives an  $^{40}\text{Ar}/^{39}\text{Ar}$  age which is less than half than the K-Ar age  
308 in Megrue et al., (1972), too great an age difference to be explained by excess Ar and probably  
309 due to separate samplings from two intimate populations of dikes at this locality.

310

## 311 4.2 Major and Trace Element Geochemistry

312 On the basis of their trace element geochemistry (see supplemental data tables), the dikes  
313 of the western Afar margin at latitude  $11^\circ\text{N}$  can be divided into four groups.

314

### 315 *4.2.1 Groups 1 and 2 dikes (~31 – 27 Ma).*

316 Group 1 dikes (~30-27 Ma) are ankaramitic dolerites. They strike NNE and are  
317 concentrated in the eastern part of the Combolcha-Batie sector. They are chemically defined by  
318 lower REE in comparison to other groups, particularly for LREE, and low LREE/HREE ratios

319 that lead to an overall less steep REE profile (Fig. 2). Low concentrations characterize the  
320 extended trace-element plot, with diagnostic peaks for Pb, Sr and to a lesser extent, K (Fig. 3).  
321 On the basis of geochemistry, the Ethiopian (or Western) plateau has been divided into separate  
322 high- and low-titanium (HT and LT) domains (Pik et al., 1998). While this study lies well within  
323 the HT domain, Group 1 dikes have a geochemical signature that broadly resembles that of the  
324 earliest, low-titanium (LT) Ethiopian Plateau flood basalts (Kieffer et al., 2004; Beccaluva et al.,  
325 2009). Major element variation diagrams for Group 1 dolerites and LT basalts typically overlap,  
326 though  $\text{Al}_2\text{O}_3$  is significantly lower and  $\text{TiO}_2$  slightly elevated in the dolerites (Fig. 4a).  
327 Likewise, primitive mantle-normalized diagrams show that Group 1 dolerites and LT basalts  
328 exhibit very similar trace element patterns, excepting dike EKA-120, an augite-hyalokaramite  
329 with slightly higher values of Nb, Ta and Sr (Fig. 3). The more incompatible trace elements,  
330 however, are enriched in the Group 1 dolerites with respect to LT basalts of equivalent MgO  
331 content (Fig. 3).

332 Group 2 dikes (~31 Ma) occur spread across the Combolcha-Batie sector. These  
333 plagioclase-rich dolerites are distinguished by steep REE profiles and the highest  $\text{La/Yb}_{\text{CN}}$  (up to  
334 11.5) of all the Afar margin dikes. Extended trace element profiles of Group 2 dolerites have  
335 features in common with Ethiopian Plateau group 1 high-titanium flood basalts (HT-1), notably  
336 troughs for Th-U and P, and peaks for Ba and Nb-Ta (Fig. 3), consistent with the study region  
337 lying within the HT province (e.g. Pik et al., 1998). Group 2 and HT-1 samples also exhibit  
338 similar element-MgO plots (Fig. 4a), excepting elevated Sr in the dolerites that is independent of  
339 CaO (not shown). Group 2 dolerites and HT-1 basalts are distinguished from Group 2 high-  
340 titanium flood basalts (HT-2) which have more elevated  $\text{TiO}_2$  (Fig. 4a) and more depleted  
341 HREE.

342

343 *4.2.2 Group 3 dikes (<10 Ma)*

344 Group 3 dikes are restricted to the swarm east of Batie. Group 3 and Group 1 dolerites  
345 share flat REE profiles, but the former are distinguished by higher concentrations of trace  
346 elements, excepting depletions in Sr, Eu and Ti (Fig. 3). Three basalt lava flows sampled by Hart  
347 et al., (1989) from locations between Wadi Fursa and Batie, have similar trace element  
348 characteristics to our Group 3 dolerites from the same area. Compared with Quaternary basaltic  
349 lavas from the Ethiopian rift valley (Fig. 4b), Group 3 dolerites display low Al<sub>2</sub>O<sub>3</sub>. They show a  
350 closer match with the major element range defined by Djibouti Holocene basaltic lavas (Deniel  
351 et al., 1994), a match which extends to trace element abundances (Fig. 4b), especially for recent  
352 Asal Rift lavas (Deniel et al., 1994), excepting that Group 3 dolerites are more enriched in  
353 HREE. The broad geochemical similarities between the Group 3 dolerites and Quaternary Afar  
354 and Ethiopian rift basalts link to their significantly younger age compared with the Groups 1 and  
355 2 dolerites (Hart et al., 1989; this study).

356

357 *4.2.3 Group 4 dikes (~25-12 Ma)*

358 Group 4 dikes occur across the entire width of the western Afar margin at latitude 11°N.  
359 They encompass all dolerites that exhibit REE slopes intermediate between those of Groups 2  
360 and 3 (Fig. 2). Whilst extended trace element patterns for Group 4 dolerites are broadly similar to  
361 Groups 2 and 3, REE slopes are less pronounced in comparison with Group 2 samples (Fig. 2).  
362 Matching their intermediate REE characteristics, Group 4 dolerites fall chronologically between  
363 Groups 2 and 3 (~25 – 12 Ma). Two subdivisions of Group 4 are identified: REE, Ti and Y  
364 abundances are higher in Group 4a dolerites compared with Group 4b (Figs. 2; 3; 4c). Group 4a

365 dolerites were intruded during the period 20-12 Ma across the greater part of the margin. The  
366 timing coincides with the ~19-11 Ma syn-extensional Getra Kele basalts from southern Ethiopia  
367 (George and Rogers, 2002). In contrast, Group 4b dikes yield ages clustered around 24 Ma and  
368 are restricted to the Desse-Combolcha sector. These dikes are considered to be feeders for the  
369 earlier lavas of the ~22-25 Ma Gugufu shield volcano (Kieffer et al., 2004). Two isolated Group  
370 4b dikes intruded east of Batie: mingled dolerite EKA-128, and evolved alkali trachyte EKA-  
371 134.

372

### 373 4.3. Isotope Geochemistry

374 Twelve representative dolerites spanning the five chemical groups were selected for  
375 isotopic analysis (Table 4). The data plot within a three end-member mixing space defined by  
376 depleted mantle, Pan African lithosphere and the Afar plume mantle, as identified in studies of  
377 Quaternary basalts in Afar and the Ethiopian rift, and Gulf of Aden (Hart et al., 1989; Schilling  
378 et al., 1992; Deniel et al., 1994; Trua et al., 1999; Furman et al., 2006; Rooney et al., 2012a).

379

#### 380 4.3.1 Groups 1 and 2 dikes

381 Group 1 have more radiogenic Pb isotopic compositions than the LT basaltic flows, and  
382 plot close to the “C” mantle reservoir (Hanan & Graham 1996; Fig. 5). However, other isotopic  
383 systems (Sr, Nd and Hf) are not consistent with a simple derivation from this single mantle  
384 reservoir (Fig. 6, 7, 8). In contrast, our single analyzed Group 2 sample, ankaramite sill EKA-  
385 112B, exhibits less radiogenic Pb isotopes that have elevated  $^{207}\text{Pb}/^{204}\text{Pb}$  and  $^{208}\text{Pb}/^{204}\text{Pb}$  at a  
386 given  $^{206}\text{Pb}/^{204}\text{Pb}$  in comparison with HT-1 basalts from this region. These isotopic parameters



387 do, however, plot consistently within the fields defined for Oligocene magmatism in Yemen  
388 (e.g., Baker et al., 1996a).

389

#### 390 *4.3.2 Group 3 dikes*

391 Group 3 dolerites have the most radiogenic  $\epsilon_{\text{Hf}}$  and  $\epsilon_{\text{Nd}}$  (Fig. 7), and least radiogenic Sr  
392 (Fig. 6) and  $^{207}\text{Pb}/^{204}\text{Pb}$  (Fig. 5) of all the samples analyzed in this study. The Pb isotope values  
393 overlap with those of the least radiogenic Quaternary Ethiopian rift basalts (Fig. 5), but Sr is  
394 significantly less radiogenic (Fig. 6) while Hf and Nd are more radiogenic (Fig. 7). These  
395 features link Group 3 dolerites to Djibouti and axial Gulf of Aden basalts. Western Afar margin  
396 basalts of similar age-range to the Group 3 dolerites, analyzed by previous authors (Hart et al.,  
397 1989), share common trace-element characteristics. However, these basalts exhibit less-  
398 radiogenic Pb isotopic signatures and typically form a broad trend, indicating the influence of  
399 the lithosphere on the erupted compositions (Fig. 5).

400

#### 401 *4.3.3 Group 4 dikes*

402 Group 4 dolerites form an array in Pb-isotope space that indicates a substantial  
403 compositional heterogeneity between radiogenic and unradiogenic components (Fig. 5). The  
404 unradiogenic Pb component correlates with unradiogenic Nd and radiogenic Sr, interpreted here  
405 as Pan-African lithosphere. Group 4a dolerites overlap with, but do not extend to more  
406 radiogenic  $^{206}\text{Pb}/^{204}\text{Pb}$  compositions (Fig. 5) displayed by the contemporaneous Getra Kele  
407 basalts in southern Ethiopia (Stewart and Rogers, 1996; George and Rogers, 2002). Indeed,  
408 substantial heterogeneity is evident between the two, where the radiogenic end-member of the

409 Getra Kele Formation appears HIMU-like (George & Rogers, 2002), distinct from the “C”  
410 signature of the Afar plume present in all dike groups from the western Afar margin.

411

## 412 **5. Discussion**

### 413 5.1 Revised chronostratigraphy for the Desse-Eloa traverse.

414         The present study adds geochronological constraints to the existing stratigraphic record  
415 outlined for the western Afar margin at latitude 11° N (Table 1). We confirm that magmatic  
416 activity in the region commenced with voluminous fissure- and pipe-fed basalt eruptions ~31 Ma  
417 ago (Hofmann et al., 1997; Ukstins et al., 2002). The feeders for this pile comprise our Group 2  
418 dolerites. Group 1 ankaramitic dikes are coincident with a period of major crustal extension and  
419 block faulting that followed the emplacement of the thick lava pile. Between 25 and 22 Ma, a  
420 period of localized magmatic activity is represented by closely spaced Group 4b dikes, feeders to  
421 the Gugufu Formation basalts (Ukstins et al., 2002; Kieffer et al., 2004) which flowed from the  
422 plateau rim down into a small „Stage 1“ basin (Wolfenden et al., 2005).

423         Between 20 and 12 Ma, a third magmatic episode produced the Burka Formation basalts,  
424 ignimbrites and tuffs (Walter, 1980; Wolfenden et al., 2005) that accumulated in a „Stage 2“  
425 basin immediately east of Batie. While the geochemistry of our Group 4a dikes matches that of  
426 the Burka formation basalts, these dikes occur over a wider region than Wolfenden et al.’s  
427 (2005) basin. The fourth and final magmatic episode within the Desse-Eloa transect produced the  
428 Upper Miocene Fursa basalts (Justin-Visentin and Zanettin, 1974). Renamed the Dahla Series by  
429 Wolfenden et al. (2005), they accumulated in a „Stage 3“ basin at the eastern end of the transect.  
430 Wolfenden et al. (2005) assign a period of 6.6–5.3 Ma to this series, but this activity may extend  
431 back to 10 Ma (Walter, 1980; Hart et al., 1989; Deniel et al., 1994). These lavas were fed by our

432 Group 3 dikes which, however, are located in the central sector of the transect somewhat to the  
 433 west of the „Stage 3“ basin.

434

## 435 5.2 Magmatic Processes along the Western Afar margin

436 The five magmatic groups defined along the western Afar margin are distinct in terms of  
 437 REE patterns, and the origin of these patterns reflects magmatic processes active during the  
 438 evolution of the Afar rift margin. To more effectively illustrate these distinctions we have  
 439 undertaken a principal components analysis of the dolerite REE data. We have used a log-  
 440 centered transform technique to overcome the constant sum constraint inherent to this form of  
 441 statistical analysis (Aitchison, 1986).

$$442 \quad Z_i = \text{Log}(X_i/g(X_D)) \quad (1)$$

443 where:

444  $i = 1, \dots, D$ , denoting elements of interest

445  $Z_i$  is the log-centered transform for each element

446  $X_i$  is the concentration of each element,  $i$

447  $g(X_D)$  is the geometric mean of all elements of interest

448

449 Approximately 96% of the variance is accounted for within the plane of the first two  
 450 eigenvectors, and this increases to 97.8% with the addition of the third eigenvector. The first  
 451 principal component (PC-1) is most influenced by the LREE and HREE, with less control from  
 452 the MREE (Table 5), whereas the second principal component (PC-2) is dominantly influenced  
 453 by LREEs and MREE (Fig. 9). The third principal component (PC-3) is dominated by Eu, Tb  
 454 and Ce and represents anomalous enrichments or depletions in these elements (e.g. plagioclase-

455 related Eu anomaly) not accounted for by PC-1 and 2. To assess the root cause of these  
456 variations, we explore the various processes that may impact on the REE patterns.

457 To a first order, fractional crystallization of nominally anhydrous mafic gabbroic  
458 assemblages and assimilation of continental crust will elevate the LREE/HREE values in an  
459 evolving magma. PC-1 is sensitive to LREE and HREE variations and exhibits clear correlation  
460 with MgO, increasing sharply for groups 2 and 3 at ~5% MgO (see supplemental data), though  
461 no clear correlation is evident for groups 4a and 4b. These data may be interpreted to infer that  
462 below ~5% MgO, lithospheric assimilation and fractional crystallization processes control the  
463 REE behavior of these magmas. For this reason, interpretations of potential mantle processes are  
464 confined to dolerites with > 5% MgO. This minimizes (but does not eliminate) the influence of  
465 gabbroic fractionation, lithospheric assimilation (Peate et al., 2008), and the complicating effects  
466 of REE-enriched phases that may become saturated in more evolved magmas (e.g. apatite and  
467 titanite: Bachmann and Bergantz, 2008).

468 Variability in the source and degree of melting are the dominant causes of REE  
469 heterogeneity in more primitive magmas. In a continental rifting environment, the lithospheric  
470 thickness determines the upper limit of the mantle melting column (Wang et al., 2002).  
471 Decreasing lithospheric thickness means a relative increase in melt from the shallower spinel  
472 lherzolite zone and relatively less melt from the deeper garnet lherzolite zone with a concomitant  
473 change in the MREE/HREE ratios of resulting magmas. Whilst lithospheric thinning may be an  
474 important ongoing process in southern and central Ethiopia (Rooney, 2010; Rooney et al., 2011),  
475 for the northern Ethiopian rift, located above the center of the ascending Oligocene plume head  
476 (Beccaluva et al., 2009), studies of temporal variation of lithospheric thickness have shown that

477 substantial thinning must have occurred prior to or contemporaneous with the initial flood basalt  
478 event (Ayalew and Gibson, 2009).

479         In a plume-influenced environment, variable contributions from ambient upper mantle  
480 and the potentially diverse components hosted within the upwelling plume may have a  
481 significant impact on the trace element characteristics of resulting magmas. A temporal decrease  
482 in plume contribution (and a concomitant increase in role of the depleted upper mantle) should  
483 correspond to source depletion and a decrease in LREE/HREE (Schilling, 1973). On the other  
484 hand, the decrease in mantle potential temperature ( $T_P$ ) when plume-influenced mantle is  
485 replaced with ambient upper mantle reduces the degree of melting and thus holds the  
486 LREE/MREE ratio relatively constant (Tegner et al., 1998; Hanghoj et al., 2003). Smaller  
487 contributions from a mantle plume to a melting column will result in a decreasing  $T_P$ , which will  
488 also impact the MREE/HREE ratios of generated magmas. A lower mantle  $T_P$  will initiate  
489 melting at shallower depths, thereby increasing the fraction of melt generated within the spinel  
490 lherzolite field, resulting in less fractionated MREE/HREE ratios. Further complexity arises  
491 when the role of pyroxenite in an upwelling plume is considered (Sobolev et al., 2005; Sobolev  
492 et al., 2007; Herzberg, 2011). The REE characteristics of these dikes are likely the result of  
493 multiple overlapping processes, and to resolve these we must establish the temporal  
494 heterogeneity in the contribution from the Afar plume to magmatism.

495

496 5.3 Temporal evolution of geochemical reservoirs along the western Afar margin

497 5.3.1. *Geochemical reservoirs contributing to magmatism*

498         Previous studies in the region have placed constraints as to the potential geochemical  
499 reservoirs contributing to magmatism in the Ethiopian magmatic province typically by

500 examining temporally restricted portions of the province (e.g., flood basalts or Quaternary rift  
501 activity: Pik et al., 1999; Rooney et al., 2012a). The suite of dikes that erupted along the western  
502 Afar margin is spatially restricted but temporally diverse, representing a 25 Myr window on the  
503 evolution of the magmatic reservoirs contributing to magmatism at a single location. The  
504 influence of a mantle plume is observed throughout the temporal magmatic record in East Africa  
505 (e.g., Rooney et al., 2012c). In modern magmas, the isotopic signature of a mantle plume is most  
506 pronounced towards Djibouti (Schilling et al., 1992; Rooney et al., 2012a), consistent with  
507 maximum  $T_P$  values recorded in this area (Rooney et al., 2012c). Another asthenospheric  
508 reservoir that displays characteristics that are broadly similar to the source of MORB is also  
509 necessary to fully account for the magmatic heterogeneity observed in Afar and along the Gulf of  
510 Aden (Schilling et al., 1992). The Pan-African lithosphere is a ubiquitous contributor to the  
511 magmatic heterogeneity observed in the region (Hart et al., 1989; Deniel et al., 1994; Trua et al.,  
512 1999; Furman et al., 2006). For the western Afar dikes, the contribution from Pan African  
513 lithospheric end-member increases with declining MgO, and can be interpreted as lithospheric  
514 (likely crustal) assimilation by asthenospheric melts during fractional crystallization in the crust.  
515 It is the interaction of these three reservoirs that account for the majority of geochemical  
516 heterogeneities observed in regional magmas.

517         Mixing models which were developed to account for the isotopic characteristics of  
518 Quaternary basalts from the Gulf of Aden and Main Ethiopian Rift have concluded that ternary  
519 mixing is evident between the Pan-African lithosphere, a depleted component thought to  
520 represent the upper mantle MORB source beneath the Gulf of Aden, and material derived from  
521 the Afar Plume (Schilling et al., 1992; Rooney et al., 2012a). These models further revealed  
522 complex patterns of reservoir interaction requiring the hybridization of the upper mantle MORB-

523 like reservoir by mixing with foundered lithospheric materials (Rooney et al., 2012a). Using the  
524 same end-members and isotopic values, we have adopted the ternary mixing hypothesis of  
525 Rooney et al., (2012a). To simplify the visualization of ternary mixing within the multi-isotope  
526 space (Sr-Nd-Pb-Hf) occupied by our samples, we have performed a principal components  
527 analysis (Fig. 10). The majority of isotopic variance is accounted for within the plane of the first  
528 two eigenvectors (97.1%), and therefore the isotopic variation is best illustrated by a PC-1/PC-2  
529 projection. PC-1 is dominated by heterogeneity in terms of the depleted upper mantle and Pan-  
530 African lithosphere end-members. While some variance on the PC-1 plane may be the result of a  
531 hybridized upper mantle (Rooney et al., 2012a), evidence of covariance of isotopic systems with  
532 MgO highlights the role of AFC processes for the western Afar dikes. PC-2 is most affected by  
533 contributions from the Afar plume end-member (Fig. 10).

534

### 535 *5.3.2. Groups 1 and 2 dikes: flood basalt eruption and subsequent dikeing between 31 and 27 Ma*

536 Our results indicate that the single isotopically characterized sample of HT-1 basalt  
537 (Group 2; EKA-112B) contains a significant contribution from depleted mantle and Pan-African  
538 lithosphere reservoirs with relatively small contribution from the Afar plume. This observation is  
539 consistent with standard isotope plots showing. EKA-112B falls closer to the Pan-African  
540 endmember in comparison to other regional HT-1 magmas. Group 1 dolerites, while having  
541 similar trace element characteristics to LT basalts of the western plateau, differ in that they carry  
542 little of the depleted mantle component that is ubiquitous in LT basalts elsewhere. Thus dolerite  
543 EKA-120 appears to have been derived from an almost binary mixture of Afar plume and pan-  
544 African lithosphere endmembers, and both Group 1 dolerites plot closer to the “C” reservoir than  
545 any previously analyzed flood basalt (Fig. 5; 10). An important implication follows, that there is

546 a decoupling between the isotopic and trace element characteristics of the Afar mantle plume.  
547 Specifically, the isotopic characteristics of the radiogenic end-member of the Afar plume (e.g.  
548 radiogenic Pb isotopes), previously attributed only to the HT-2 basalts (Pik et al, 1999) can also  
549 be found in some LT basalts represented by our Group 1 dolerites.

550

### 551 *5.3.2 Group 4 dikes: Shield volcanism between 25 and 12 Ma*

552 Group 4b dolerites, which are related to the ~22-25 Ma Gugufu shield volcano, show  
553 evidence of mixing between the Afar plume and the pan African lithosphere components (Fig.  
554 10). We suggest that plume-derived melts assimilated Pan-African crustal materials during  
555 magma differentiation. However, identity of the plume component in the ~25-22 Ma shield  
556 basalts is debated (Kieffer et al., 2004). Previous research notes that the Choke and Gugufu  
557 basaltic shield volcanoes have more elevated Pb-isotopic values compared to the underlying  
558 Oligocene flood basalts (Kieffer et al., 2004). This isotopic heterogeneity is mirrored in the trace  
559 element characteristics, where the 25-22 Ma basalts bear similarities to Quaternary basalts in the  
560 Ethiopian rift and the northern Kenyan rift (Furman et al., 2004; Furman et al., 2006). The  
561 radiogenic end-member in the shield basalts of the western Ethiopian plateau has been  
562 interpreted to be a HIMU-like component within a complex upwelling (Kieffer et al., 2004),  
563 though the Pb isotopic values of these shield volcanoes lie close to the “C” mantle reservoir (Fig.  
564 5). Hf isotopic data in this study preclude a dominantly HIMU-like component in the western  
565 Afar dikes, and instead favor derivation from a “C”-like reservoir (Fig. 7; 8) similar to that for  
566 the Oligocene flood basalts (Marty et al., 1996; Furman et al., 2006).

567 From our data it is apparent that from ~30 to 22 Ma, the depleted mantle did not play a  
568 significant role in magma generation (Fig. 5), and as a result, the Pb isotope signature in basalts



569 throughout this period reflects mixing between an endmember composed almost entirely of the  
570 Afar plume and the Pan African lithosphere. The modest degree of magmatism during this period  
571 (isolated shield volcanoes and dikes) argues against an increased plume flux in comparison to the  
572 initial flood basalt eruptions. However, potentially fertile and warm plume material located in the  
573 upper mantle that perhaps had not participated in melting during the initial flood basalt event or  
574 were part of a complex upwelling (Kieffer et al., 2004; Bastow et al., 2008; Rooney et al., 2012c)  
575 might be expected to melt preferentially as modest extension commenced along the Afar margin.

576         The 20-12 Ma interval represented by Group 4a dolerites in the Desse-Eloa transect  
577 correlates with a period of reduced basaltic volcanism around Afar, and coincided with ongoing  
578 lithospheric extension throughout the region. In addition to rifting along the western Afar  
579 margin, rifting at this time occurred in southern Ethiopia (Bonini et al., 2001), whilst sea-floor  
580 spreading was initiated in the Gulf of Aden and Red Sea (Bosworth et al., 2005, and references  
581 therein). The Group 4a dikes were therefore injected during an important dynamic phase in  
582 regional development of extension of the Afar margins. Group 4a dolerites plot close to the  
583 binary mixing region between Pan African lithosphere and the depleted mantle end-members  
584 (Fig. 5; 10), implying a lesser contribution from the Afar plume, in sharp contrast to the 30-22  
585 Ma time period (Fig. 5).

586

### 587 *5.3.3 Group 3 dikes: Evolution of rifting from 10 Ma to Recent*

588         The period commencing at ~10 Ma marked the initiation of rifting in the northern  
589 Ethiopian rift and the eventual connection of the rift basins in Afar and central Ethiopia (Kazmin  
590 et al., 1981; Bonini et al., 2005; Wolfenden et al., 2005; Corti, 2009). Trace element and isotopic  
591 characteristics of Group 3 dolerites indicate a more significant contribution from the depleted

592 mantle in their petrogenesis in comparison to other groups (Fig. 2; 5; 7; 8; 10). While this  
593 component is of the same magnitude as in Group 4a dolerites (e.g., EKA-106), the two are  
594 distinguished by smaller lithospheric contributions in the Group 3 dolerites (e.g., Fig 10). Our  
595 data confirm previous studies on Afar margin lavas which show that, with decreasing age, the  
596 isotopic properties of the basalts express a more-depleted composition. This is interpreted simply  
597 as an increased contribution from the depleted upper mantle and a lessening of crustal  
598 assimilation (Hart et al., 1989). A similar pattern is observed in Djibouti where early volcanic  
599 products (>10 Ma) exhibit substantial lithospheric contributions, but which become insignificant  
600 as rifting and lithospheric thinning progress, replaced by an increasing fraction of melt derived  
601 from depleted upper mantle and the Afar plume (Deniel et al., 1994).

602

#### 603 5.4 Rift evolution at the western Afar margin and comparisons to East Greenland

604

605 Tectonic thinning alone is an inadequate mechanism to explain the evolution of the East  
606 African Rift System (Berckhemer et al., 1975; Mohr, 1983b). The concept that magmatic  
607 intrusions can significantly weaken the continental lithosphere, leading ultimately to its rupture,  
608 is now widely accepted in hypotheses of rift evolution (Klausen and Larsen, 2002; Buck, 2004;  
609 Buck, 2006; Bialas et al., 2010). The best exposed example of magma-rich breakup is the East  
610 Greenland continental margin, where glacier-cleared exposure reveals a regional pattern of  
611 diking, faulting and warping in a breakup zone initiated over a mantle plume (Myers, 1980;  
612 Klausen and Larsen, 2002; Hanghoj et al., 2003). The dikes along the western Afar margin share  
613 many of the same characteristics of the East Greenland dike swarm. The East Greenland swarm  
614 is broadly divided into an early stage of mafic diking that compositionally correlates with the

615 regional flood basalt sequences, and a later less MgO-rich period of diking that does not correlate  
616 with the erupted flood basalts (Hanghoj et al., 2003). Similar to these observations, early dikes  
617 from western Afar are compositionally related to the regional flood basalt sequences and are  
618 relatively mafic. Later dikes from western Afar are similar to those from east Greenland that are  
619 typically less mafic and have no extrusive equivalent within the flood basalt sequence.

620 Statistical treatment of more than 1400 dikes (Klausen and Larsen, 2002) documents a  
621 progressive shift in orientation from predominantly subvertical inland to predominantly landward  
622 dipping (as low as 40°) offshore. This expresses the progressive seaward rotation of crustal units  
623 during the evolution of the margin (Morton and Black, 1975). Exposed dikes in the Afar margins  
624 are an order less numerous than in East Greenland. Nevertheless they share the same plateau-  
625 ward/inland dip, although an eastward decrease in the riftward dip angle of increasingly more  
626 abundant dikes is not observed along the Dessie-Eloa transect (cf. Wolfenden et al., 2005),  
627 perhaps a result of the cover of younger lavas in the easternmost part of the transect.

628 Our interpretation of the tectonic and magmatic evolution of the western Afar margin  
629 follows the three-stage rifting process proposed by Buck (2006): an initial stage of voluminous  
630 magmatic intrusion, an intermediate stage dominated by tectonic stretching, and a final stage  
631 where focused magmatic intrusion dominates strain accommodation:

632

#### 633 *5.4.1 Stage 1: Voluminous magmatic intrusion*

634 The initial stages of rifting coincide with the emplacement of melt at various levels  
635 within the lithosphere. Depending on the supply of magma, not all dikes may attain the surface.  
636 However, even small volumes of magma at the early stage of rift development may have a  
637 significant impact in subsequent rift evolution (Bialas et al., 2010). Within our study region the

638 Group 2 dikes, related to the initial plume-head impact, strike rift-parallel precisely as predicted  
639 by models of initial magma-assisted rifting (Buck, 2006). The Ethiopian Oligocene flood-basalt  
640 pile attests to the enormous volumes of magma available to assist initiation of Afar margin  
641 rifting (Fig. 11A). The African lithosphere is considered to have a typical thickness of 120 km  
642 (Dugda et al., 2007), which requires some preliminary thinning process to have occurred before  
643 rifting could commence (Bialas et al., 2010). Existing studies (e.g., Ayalew & Gibson 2009),  
644 provide evidence that the necessary lithospheric thinning under Afar occurred during the impact  
645 of the Afar plume, perhaps from transformation and erosion at the base of the lithosphere,  
646 although the extent and magnitude of this thinning remain uncertain.

647

#### 648 *5.4.2 Stage 2: Tectonic stretching*

649 The second stage of rifting was characterized by a shift towards a greater degree of  
650 lithospheric stretching and faulting, proceeding rapidly in regions where previous magmatic  
651 injection had been voluminous (Bialas et al., 2010). Tectonic extension dominated this stage,  
652 while magmatism was greatly reduced. Whereas the initial, Oligocene flood-basalt event is well-  
653 represented in both Ethiopia and Yemen, the subsequent rifting of the African-Arabian continent  
654 involving the drift of Arabia away from the Afar plume reduced volcanic activity on the eastern  
655 flank of the Red Sea rift (Ukstins et al., 2002). In contrast, the western Afar margin preserves  
656 evidence of a wide temporal range of magmatic products, and offers insight into the relationship  
657 between magmatism and extension along an evolving rift margin. The diking associated with  
658 continued extension along the western Afar margin can be broadly divided on the basis of  
659 geochemistry into two events, represented by Group 4b dikes (Fig. 11B; 25-22 Ma), and Group  
660 4a dikes (Fig. 11C; 20-12 Ma). They confirm that stretching and faulting of the western Afar

661 crust was accompanied by local volcanism and magmatically induced subsidence that  
662 progressively moved riftwards with time (Fig 11C: Wolfenden et al., 2005).

663         Local diiking and volcanism following the initial rifting of the Red Sea margin (Group 4b  
664 dikes; 25-22 Ma) was located at the rift border fault on the Desse-Eloa transect and fed  
665 construction of the Guguftu shield volcano on the plateau rim (Fig 11B: Kieffer et al., 2004;  
666 Wolfenden et al., 2005). Further riftward migration of strain was accompanied by local diiking  
667 and volcanism (20-12 Ma), significantly closer to Afar (Fig 11C: Justin-Visentin and Zanettin,  
668 1974; Morton et al., 1979). Nevertheless, a simple model of the younging of dikes towards the  
669 rift zone is complicated in the western Afar margin by overprinting. Contemporaneous lavas  
670 along the rift margin have a magmatic signature in common with the Desse-Eloa dolerites,  
671 revealing the assimilation of continental lithosphere by asthenosphere-derived basaltic magmas  
672 (e.g., Fig. 5, 10), and the generation of a significant volume of silicic magmas (erupted as  
673 ignimbrites) derived by fractional crystallization of the same basalts (Ayalew and Gibson, 2009).

674         The increase in silicic volcanism during the 20-12 Ma period was related to the ongoing  
675 lithospheric extension. Fractional crystallization of basaltic magma rather than anatexis of  
676 continental crust was the major source for the silicic magmas of the Afar and rift valley margins  
677 (Ayalew et al., 2002; Peccerillo et al., 2003; Peccerillo et al., 2007; Ayalew and Gibson, 2009;  
678 Rooney et al., 2012b). A lessened magma supply rate, resulting in magmatic intrusion at greater  
679 depths and slower cooling (Behn et al., 2006), fostered crystal fractionation processes together  
680 with lithospheric assimilation. Additionally, rift faulting and fissuring within the continental  
681 crust facilitated shallow-level magmatic intrusion and differentiation (Antonellini and Cambray,  
682 1992), together with stagnation of laterally migrating magma in the footwall of the faults (Bonini  
683 et al., 2001). Volcanic periodicity may reflect the complex relationship between magma

684 chamber size, supply rate, and crystallinity (Jellinek and DePaolo, 2003). In rift margin  
685 environments, variations in the modeled strain field of a flexing plate (whereby melt at the base  
686 of the crust travels to the surface through fractures: Ellis and King, 1991) might also account for  
687 some degree of the periodicity of volcanism, allowing longer magma storage in the continental  
688 crust under the rift flanks. Accumulation of magma in the footwall of a rift border-fault can  
689 produce a feedback whereby rheology changes reduce the strength of the lithosphere, in turn  
690 resulting in a period of further faulting and intrusion (Bonini et al., 2001).

691

#### 692 *5.4.3 Stage 3: strain accommodation by magmatic intrusion*

693 In the third and final stage of rift development, extension became focused at the rift axis  
694 (Mohr, 1978; Bilham et al., 1999; Ebinger and Casey, 2001; Casey et al., 2006; Rooney et al.,  
695 2011), manifested as intensive diking through severely thinned lithosphere (Ebinger and Casey,  
696 2001; Buck, 2004; Keranen et al., 2004; Wolfenden et al., 2005; Buck, 2006; Maguire et al.,  
697 2006). At this stage (<10 Ma), the western Afar margin was the site of local volcanism on a scale  
698 of segmentation similar to that of stage 2 but migrated closer to the rift floor (Fig. 11D). Group 3  
699 dikes samples have a significantly weaker lithospheric signature in comparison to Group 4a  
700 dikes, consistent with asthenospheric reservoirs becoming progressively more important in  
701 controlling the isotopic compositions of basaltic magmas as the rift margin evolved and  
702 magmatic injection became more focused (Hart et al., 1989; Deniel et al., 1994).

703 Our results show a temporal variation in the contribution of the Afar plume and depleted  
704 mantle to western Afar magmas, defined by an initial strong plume signature (Groups 1 and 4b)  
705 that becomes less pronounced in the later groups (Groups 3 and 4a; Fig. 10). Modest lithospheric  
706 thinning during the later development of the continental rift margin, from 20 Ma onward,

707 facilitated decompressional melting of the depleted upper mantle (Figs. 5, 10). Initially the  
708 western Afar margin at latitude 11° N was situated close to the center of the Afar plume during  
709 the flood-basalt event and initial rifting (Beccaluva et al., 2009), but continued lithospheric  
710 extension and the formation of new rift lithosphere then shifted the margin away from the plume  
711 center which is now located under Lake Abhe in central Afar (Schilling et al., 1992). The  
712 significant spatial heterogeneity among the late Cenozoic asthenospheric reservoirs contributing  
713 to magmatism beneath Djibouti and western Afar is surprising, considering the short distance  
714 (170 km) between the two regions (Schilling et al., 1992). It may reflect a progressively greater  
715 dispersion and preferential channeling of the Afar plume beneath the extending lithosphere  
716 (Sleep, 2008), which is consistent with geochemical, bathymetric, gravity, magnetic, and  
717 magneto-telluric data from the Gulf of Aden and Main Ethiopian Rift (Schilling et al., 1992;  
718 Leroy et al., 2010; Rooney et al., 2012a).

719

## 720 **6. Conclusions**

721 The western margin of Afar was formed by lithospheric and crustal extension accompanied by  
722 major diking and volcanism during the Oligocene to Quaternary evolution of the Afar rift basin.  
723 Magmatic activity, though varying in intensity throughout this evolution, spanned the entire  
724 history of the progressive continental rifting that formed the margin. Dike and lava samples from  
725 the margin now provide a window into the mantle sources and reservoirs involved, and the  
726 interaction and changing contributions from Afar plume, African lithosphere and depleted upper  
727 mantle melts. New  $^{40}\text{Ar}/^{39}\text{Ar}$ -geochronology places further constraints on the magmatic events of  
728 the margin, in which five broad episodes are revealed:

- 729 1) The earliest dikes were contemporaneous with the 31 – 29 Ma flood-basalt province that  
730 covered much of Ethiopia and western Yemen (Fig. 11a). The geochemistry of these  
731 dikes resembles that of the HT-1 flood basalt flows which they intruded, though the dikes  
732 extend to significantly more mafic compositions (up to 12% MgO). The impact of the  
733 Afar mantle plume head at ~31 Ma initiated thinning of the overlying lithosphere and  
734 promoted melting of the depleted mantle and African lithosphere, generating magmas  
735 that were a broad mix of all three geochemical reservoirs.
- 736 2) From ~30 to 27 Ma, a second, less intense stage of diking coincided with a broad lull in  
737 volcanic activity across the margin (Fig. 11b). The trace-element geochemistry of these  
738 dikes resembles that of the LT flood basalts, but isotopes reveal that the dikes magmas  
739 contained a significantly elevated plume component compared with flood basalt magmas  
740 erupted elsewhere on the western Ethiopian plateau.
- 741 3) From 25 to 22 Ma, formation of the Gugufu and Choke basaltic shields on the adjacent  
742 plateau coincided with a significant increase in margin diking (Fig. 11b). The basalts and  
743 dolerites share a similar geochemistry. The Afar plume contributed significantly to these  
744 magmas, although assimilation of African lithosphere (likely crust) supplied the  
745 heterogeneity evident in the radiogenic isotopic values. The minimal presence of a  
746 depleted mantle component from ~30 to 22 Ma could be the result of limited mantle  
747 upwelling due to the inferred small degree of lithospheric thinning during this time  
748 period.
- 749 4) From 20 to 12 Ma, the evolving rift margin drifted away from the site of the plume.  
750 Decompressional melting of the depleted mantle became an important melt generation  
751 mechanism for the dike magmas as extension proceeded, though contributions from the



752 Afar plume persisted. Widespread silicic magmatism across the margins of Afar was  
753 coincident with a spread of mafic diking (Fig. 11c) carrying a significant lithospheric  
754 component.

755 5) The final stage of margin diking commenced at ~10 Ma. It coincided with the  
756 development of a spread of oblique faulting across the margin, and a narrow rift-parallel  
757 graben adjacent to the plateau (Fig. 11d). Magmatic intrusion was focused at two  
758 locations: at the easternmost sector of the margin, and in the marginal graben. Dikes and  
759 magmas of this period, like the preceding period, had a significant contribution from the  
760 depleted, asthenospheric mantle. However, further maturation of the margin led to a more  
761 established magmatic plumbing system at the riftward edge of the margin leading to a  
762 diminished lithospheric contribution to magmas of this period.

763

## 764 **Acknowledgements**

765 The authors wish to thank Matthew Parsons, Chelsea Mack, Tim Matthews, Thomas Hudgins  
766 and Christian Briggs who assisted with sample preparation and analysis. Emmanuel Ponzevera  
767 performed the Neptune ICMPS measurements for Pb, Nd and Hf isotopes. PM expresses  
768 gratitude to Professor Pierre Gouin, S.J., for vital support at base during the original field  
769 mapping and sampling of the western Afar margin dikes in 1969. TR thanks Clifton Rooney for  
770 assistance with figures. Discussions with Dan McKenzie and Eric Grunsky assisted in our data  
771 interpretation. We thank Wendy Nelson, Cindy Ebinger, Ian Bastow, and Derek Keir for  
772 comments that improved the manuscript. Ingrid Uskins-Peate, Karen Hanghøj, and an  
773 anonymous reviewer provided detailed and helpful reviews which enhanced the manuscript.  
774 Finally we thank Steve Shirey for careful editorial handling.

775

776 **FIGURE 1.**

777 Spatial distribution of dike samples throughout the region. The approximate alignment of the  
778 Desse-Eloa highway is shown for reference. Topography is a digital elevation model based on  
779 the NASA/JPL SRTM dataset. The structural basins outlined by Wolfenden et al., (2005) are

780 outlined: stage 1 basin – dark grey filling, stage 2 basin – dotted fill, stage 3 basin – vertical  
 781 lines. Additional samples presented in Hart et al., (1989) are also shown. Towns referred to in the  
 782 text are denoted by stars. A) Inset region is topography of the Afar triple junction region showing  
 783 the broad structural features including the Main Ethiopian Rift, Red Sea, and Gulf of Aden; B)  
 784 Inset of the regional tectonic framework focusing on structural basins (labelled 1-3; Wolfenden  
 785 et al., 2005). Pliocene-Quaternary basaltic magmatism within the Ethiopian rift is also shown for  
 786 reference (Rooney et al., 2011); C) Dikes less from ~20 to 6 Ma (Groups 3, 4a); D) Dikes from  
 787 31 to 24 Ma (Groups 1, 2, 4b).

788 FIGURE 2

789 Chondrite normalized (Boynnton, 1984) rare earth element pattern outlining the variation among  
 790 the different dike groupings. The low trace element abundance of group 1 dikes is particularly  
 791 apparent. Also of note are the low and elevated values of HREE in groups 2 and 3 respectively.  
 792

793 FIGURE 3

794 Primitive mantle normalized (Sun and McDonough, 1989) trace element diagrams of dike groups  
 795 1 – 4. Contemporaneous basalts are shown as shaded backgrounds for each group.

796 a. Low-Ti (LT) basalts from our study area (group 1) in comparison to other LT basalts  
 797 from the western Ethiopian plateau (Pik et al., 1999; Kieffer et al., 2004; Beccaluva et al.,  
 798 2009). Group 1 samples plot within the range of other western plateau samples and  
 799 exhibit a similar trace element pattern.

800 b. High-Ti type 1 (HT-1) basalts from group 2 are plotted with HT-1 samples from the  
 801 western Ethiopian plateau (Pik et al., 1999; Beccaluva et al., 2009). Patterns between  
 802 both series broadly correlate though group 2 samples extend to depleted values of the

- 803 more compatible elements, and higher values of Nb-Ta in comparison to other HT-1  
804 basalts.
- 805 c. Group 3 basalts are shown in comparison to Quaternary volcanic rocks from the Main  
806 Ethiopian Rift (Rooney et al., 2005; Furman et al., 2006; Rooney et al., 2007; Rooney,  
807 2010). Our group 3 differs markedly from the Quaternary rift-floor volcanic in the MER  
808 by having much more enriched values of HREE and an overall flatter trace element  
809 profile.
- 810 d. Group 4a samples are plotted against contemporaneous Getra Kele rift margin basalts of  
811 southern Ethiopia (George and Rogers, 2002). While group 4a plots with the Getra Kele  
812 basalts in terms of the more incompatible elements, there is a distinct heterogeneity  
813 between the two in terms of the more compatible elements – group 4a samples are  
814 significantly more enriched.
- 815 e. Group 4b samples which likely are related to the Gugufu shield volcano are plotted  
816 against the two volcanic shields which have developed at this time (Gugufu and Choke;  
817 Kieffer et al., 2004). Group 4b overlaps with Gugufu basalts in terms of the more  
818 incompatible elements but display significant heterogeneity in terms of K, Th, and U.  
819 These variations may reflect lithospheric assimilation evident in the radiogenic isotope  
820 properties of these rocks.

821

## 822 FIGURE 4

- 823 a. MgO-X diagrams illustrating the variance between different Oligocene basalts in  
824 Ethiopia (Pik et al., 1999; Kieffer et al., 2004; Beccaluva et al., 2009) and Yemen (Baker  
825 et al., 1996b).
- 826 b. MgO-X diagrams illustrating the variance between our group 3 and the 10 Ma- Recent

827 activity in MER of Ethiopia (Rooney et al., 2005; Furman et al., 2006; Rooney et al.,  
 828 2007; Rooney, 2010), Pliocene-Quaternary Djibouti, Quaternary Asal Rift, and 4-9 Ma  
 829 Dahla series (Deniel et al., 1994).

830 c. MgO-X diagrams illustrating the variance between the rift margin and shield building  
 831 phase of the Ethiopian plateau and group 4 of this study. We show that group 4a (19-12  
 832 Ma) is distinct from the contemporaneous Getra Kele formation of southern Ethiopia in  
 833 most element plots (Stewart and Rogers, 1996; George and Rogers, 2002). The distinct  
 834 major element trends (e.g.  $\text{CaO}/\text{Al}_2\text{O}_3$ ) reflect the unusually deep clinopyroxene-  
 835 dominated fractionation of the Getra Kele basalts (George and Rogers, 2002). Group 4b  
 836 displays a similar range in trace elements when compared to the 22-25 Ma Choke and  
 837 Gugufu shield volcanoes (Kieffer et al., 2004). Groups 4a can be distinguished easily  
 838 from group 4b, and displays elevated Zr.

839 FIGURE 5.

840 Pb isotope variation plot showing our samples and other similar units in the region. A)  
 841  $^{208}\text{Pb}/^{204}\text{Pb}$  versus  $^{206}\text{Pb}/^{204}\text{Pb}$ . B)  $^{207}\text{Pb}/^{204}\text{Pb}$  versus  $^{206}\text{Pb}/^{204}\text{Pb}$ . Group 3 dikes are shown along  
 842 with contemporaneous samples from western Afar reported by Hart et al., (1989). Data sources  
 843 are: Getra Kele (Stewart and Rogers, 1996; George and Rogers, 2002); Choke/Gugufu (Kieffer  
 844 et al., 2004); Djibouti includes Dahla, Asal rift and Pliocene-Quaternary basalts (Schilling et al.,  
 845 1992; Deniel et al., 1994); MER - Main Ethiopian Rift (Furman et al., 2006; Rooney et al.,  
 846 2012a); Gulf of Aden (Schilling et al., 1992); Yemen (Oligocene) (Baker et al., 1996b); western  
 847 plateau HT1/HT2/LT (Pik et al., 1999; Kieffer et al., 2004). All data (our newly presented and  
 848 existing data) older than ~10 Ma is age corrected. "C" is the mantle reservoir outlined by Hanan  
 849 & Graham (1989) and the assumed composition of the Afar Plume (Furman et al., 2006). Afar  
 850 Plume, DM (depleted mantle) and PA (Pan African lithosphere) are endmembers modelled to

851 contribute to magmatism in the region (Schilling et al., 1992; Rooney et al., 2012a). The northern  
852 hemisphere reference line (NHRL: Hart, 1984) is also drawn.

853 FIGURE 6

854  $^{143}\text{Nd}/^{144}\text{Nd}$  vs  $^{87}\text{Sr}/^{86}\text{Sr}$  variation for samples within this study and other similar units in the  
855 region. Endmembers and other regional datasets are those outlined in the caption of figure 5.  
856 Note that all isotopes are age corrected except those less than ~10 Ma. Group 1 overlaps the  
857 values for Yemen, plotting at more radiogenic Sr and unradiogenic Nd in comparison to most  
858 regional LT basalts, and consistent with an assimilation model. The single Group 2 dike plots  
859 near to the Yemen field. It is apparent that our group 4b data broadly overlap Choke/Gugufu at  
860 the less radiogenic values of  $^{87}\text{Sr}/^{86}\text{Sr}$  but fall at a slightly more radiogenic value for  $^{143}\text{Nd}/^{144}\text{Nd}$ .  
861 Group 4b extends towards extremely radiogenic  $^{87}\text{Sr}/^{86}\text{Sr}$ , values typical of lithospheric  
862 contributions. Group 4a samples plot in a similar array but are displaced to lower values of  
863  $^{143}\text{Nd}/^{144}\text{Nd}$ .

864 FIGURE 7

865 Variation of samples from this study shown with a field outlining the only other data suites in the  
866 region that includes Hf isotopes. The undifferentiated Oligocene-Miocene western plateau  
867 basalts and Quaternary western plateau basalts presented by Meshesha et al., (2007; 2010) are  
868 shown here for reference. We also include Quaternary data from the Gulf of Aden and Main  
869 Ethiopian Rift (Rooney et al., 2012a). Trends shown in this plot broadly reflects other isotopes  
870 systems – groups 1 and 2 lie above the mantle array. In contrast group 4b samples plot at or  
871 below the mantle array with increasing contributions from the Pan African endmember. This  
872 pattern is mirrored by the Miocene-Oligocene and Quaternary samples from the western plateau  
873 which extend to lower  $\epsilon_{\text{Hf}}$  at the more differentiated end of the mixing array. While the precise  
874 value of  $\epsilon_{\text{Hf}}$  for the PA endmember remains unclear, it is lower than the mantle array. Group 3

875 samples are more radiogenic than the “C” mantle reservoir, consistent with an increased role for  
876 the depleted mantle component in their genesis.

877

878 FIGURE 8

879  $\epsilon_{\text{Hf}}$  shown against  $^{206}\text{Pb}/^{204}\text{Pb}$  isotopes for samples from this study and other regional data suites  
880 (see Figure 7 for data sources). This isotopic projection rules out a significant contribution from  
881 a HIMU-like reservoir in the petrogenesis of any of our samples. Furthermore, data from the  
882 undifferentiated Miocene-Oligocene western plateau rocks (which appear to extend towards  
883 HIMU in an  $\epsilon_{\text{Hf}}-\epsilon_{\text{Nd}}$  projection) are displaced towards unradiogenic Pb isotopes.

884

885 FIGURE 9.

886 A) Score plot from our principal component analysis (PCA) of the REEs in our dike  
887 samples. See Table 5 for the details of PC1, 2 and 3. Dike groups are particularly  
888 apparent in this projection. See the main text and Table 5 for more details of the PCA  
889 analysis and description of the results.

890 B) REE ratio plot after Hanghøj et al., (2003). Samples approximately >5% MgO are shown  
891 here and values have been normalized to C1 chondrite. This projection illustrates the  
892 relative enrichment of LREE to MREE (La/Sm) and MREE to HREE (Dy/Yb).

893 FIGURE 10

894 Score plot from our PCA of the isotopic values for our dike groups 1-4. This principal  
895 component analysis included  $\epsilon_{\text{Hf}}$ ,  $\epsilon_{\text{Nd}}$ , and Sr in addition to the three Pb isotopes. Endmembers  
896 are: “C” – Afar plume, DM – depleted mantle, PA – Pan African lithosphere. The endmember

897 values are listed in Table 6. PC-1 records the relative contributions from the DM and PA  
898 reservoirs while PC-2 reflects the contributions from the radiogenic “C” endmember interpreted  
899 as the Afar Plume. The general restriction of data to within the plane of these two eigenvectors is  
900 consistent with a ternary mixing model. The most radiogenic endmember of group 4b may  
901 extend to outside of this mixing array, though heterogeneity in the plume endmember is likely.  
902 Samples from other studies (e.g. Hart et al., 1989) could not be plotted with this method as PCA  
903 requires each sample to have the same number of data values – no Hf data is available for most  
904 older datasets.

#### 905 FIGURE 11

906 Cartoon outlining a potential model for the evolution of the western Afar margin. These cartoons  
907 do not show contemporaneous activity within the rift (e.g., Rooney et al., 2011). See the text for  
908 a full narrative.

909

#### 910 TABLE 1

911 Summary of the existing stratigraphic groups defined by Wolfenden et al., (2005).

#### 912 TABLE 2

913 Summary of dike and fault trends across the Afar margin between Desse and Eloa, presented in  
914 detail elsewhere (Mohr, 1971).

#### 915 TABLE 3

916  $^{40}\text{Ar}/^{39}\text{Ar}$  geochronology results. Samples EKA-120 and EKA-119 were irradiated in package  
917 number mc23, samples EKA-111 and EKA-112B were irradiated in package mc24 and samples  
918 EAD-114, EKA-140A and EKA-153 were irradiated in package mc25. Packages mc23 and mc24

919 were each irradiated for 15 hours (45 MWh) while package mc25 was irradiated for 2 hours (6  
920 MWh). Standard hornblende MMhb-1 was used as the fluence monitor for packages mc23 and  
921 mc24. Fish Canyon Tuff biotite split 3 (FCT-3) was used as the fluence monitor for package  
922 mc25. The K-Ar age of 520.4 Ma was used for MMhb-1 in calculating J values (Samson and  
923 Alexander, 1987) and an age of 27.99 Ma was used for FCT-3, which is a value previously  
924 calibrated against MMhb-1 (Hall and Farrell, 1995). For each sample, a total gas age (TGA) was  
925 calculated by adding up all of the gas fractions for a sample run. This age should most closely  
926 mimic what would be expected from a conventional K-Ar age. In addition to the TGA values,  
927 when possible, an error weighted plateau age (EWP) was also calculated. Plateau segments were  
928 selected based on the following criteria: a) there are a minimum of 3 contiguous gas fractions  
929 constituting at least 50% of the  $^{39}\text{Ar}$  released; and b) the error weighted mean of the segment  
930 passes the null hypothesis that the calculated ages are all equal using a  $\chi^2$  test at the 95%  
931 confidence level. When multiple plateau segments were available, the one with the minimum  
932 error estimate was chosen. EWP ages include the effects of scatter about the error weighted mean  
933 age. Given that the samples analyzed were whole-rock samples with fine-grained inclusions  
934 having contrasting K-concentrations, the  $\sim 80\text{nm}$  recoil distance expected for  $^{39}\text{Ar}$  might be  
935 expected to contribute a significant amount to variations in ages within an age spectrum (Turner  
936 and Cadogan, 1974). Specifically, if K-rich phases donate  $^{39}\text{Ar}$  into neighboring K-poor sites,  
937 then if the different minerals degas at different temperatures, one would expect anomalously high  
938 ages in the K-rich minerals and anomalously low ages in the K-poor ones. In order to account for  
939 this, while still eliminating low temperature gas fractions with apparent Ar loss due to alteration  
940 and/or diffusion, Turner et al., (1978) used the concept of a “reduced plateau” age which is  
941 calculated by totaling the gas over the fractions that would have exhibited plateaus without  $^{39}\text{Ar}$



942 recoil artifacts. In order to avoid confusion with the normal terminology of error weighted  
943 plateaus, we refer to these ages as reduced integrated ages (RIA), as they are calculated by  
944 integrating the gas release over a portion of the age spectrum. A combined isochron age (CIA)  
945 was calculated by combining the gas fractions for all of a sample's replicate analyses. Scatter  
946 about the best fit line was included in the CIA error estimate. Details of the isochron fits as well  
947 as the fractions used in the EWP and RIA ages are given in the supplementary material. In the  
948 case of TGA, EWP and RIA ages, an error weighted average of the ages was calculated to  
949 provide an overall sample age estimate. The TGA, EWP, RIA and CIA model age errors all  
950 include the uncertainty in J. One of the 4 model ages was chosen as a "preferred" age and the  
951 reasons for the choice of preferred age are outlined below. Laser fusion system blanks were  
952 monitored regularly (typically every 5<sup>th</sup> sample gas fraction) and typical measured blanks at  
953 masses 36, 37, 38, 39, and 40 were about  $4 \times 10^{-14}$ ,  $4 \times 10^{-14}$ ,  $4 \times 10^{-15}$ ,  $4 \times 10^{-14}$ , and  $7 \times 10^{-12}$  ccSTP  
954 respectively.

955

## 956 TABLE 4

957 Isotopic characteristics of dikes along the Desse-Eloa transect. All Hf, Pb and Nd isotope  
958 measurements were made on a Thermo Neptune multi-collector inductively coupled plasma  
959 mass spectrometer at Ifremer. Repeat measurements of the Hf isotope standard JMC 475 during  
960 the course of the analyses yielded reproducibility of 46ppm ( $2\sigma$ ) on  $^{176}\text{Hf}/^{177}\text{Hf}$  with a value of  
961 0.282165. The Pb isotope data are reported relative to published values for NBS 981 in  
962 Catanzaro et al., (1968). The samples were spiked with thallium to correct for mass fractionation.  
963 Based on repeated runs of NBS 981 during the course of the analyses, the estimated external  
964 precision for Pb analyses is  $\pm 0.02\%$ ,  $2\sigma$  for  $^{206}\text{Pb}/^{204}\text{Pb}$  and  $^{207}\text{Pb}/^{204}\text{Pb}$  and  $\pm 0.03\%$ ,  $2\sigma$  for

965  $^{208}\text{Pb}/^{204}\text{Pb}$ . Repeat measurements of the Nd isotope standard JNdi-1 (Tanaka et al., 2000)  
 966 yielded  $^{143}\text{Nd}/^{144}\text{Nd}$  values of  $0.512114 \pm 12$  ( $2\sigma$ ,  $n=8$ ). Sr isotope measurements were performed  
 967 on a multicollector Finnigan MAT26X mass spectrometer upgraded by Spectromat. Replicate  
 968 analyses of NBS 987 during the analysis period gave an average value of  $0.71025 \pm 3$  ( $2\sigma$ ,  $n=9$ ).  
 969 Analysis of BCR-2 gave Hf-Pb-Sr-Nd values of  $^{176}\text{Hf}/^{177}\text{Hf} = 0.282861 \pm 9$ ,  $^{206}\text{Pb}/^{204}\text{Pb} =$   
 970  $18.7528 \pm 6$ ,  $^{207}\text{Pb}/^{204}\text{Pb} = 15.6203 \pm 6$ ,  $^{208}\text{Pb}/^{204}\text{Pb} = 38.7355 \pm 19$ ,  $^{87}\text{Sr}/^{86}\text{Sr} = 0.705007 \pm 7$ ,  
 971  $^{143}\text{Nd}/^{144}\text{Nd} = 0.512639 \pm 4$  respectively.

972 TABLE 5

973 Eigenvectors from our principal components analysis of the REE patterns in our groups 1 to 4.  
 974 For details of the analysis and interpretations refer to the text.

975 TABLE 6

976 Endmember compositions used in plotting and for principal components analysis. For Sr, Nd,  
 977 and Pb the isotopic values for the depleted mantle and Pan African lithosphere endmembers are  
 978 identical to Schilling et al., (1992). The Afar plume composition is set as the “C” mantle  
 979 reservoir of Hanan & Graham, (1996). To facilitate incorporating the Hf isotopic system into our  
 980 interpretations, we make the assumption that the Afar plume and the regional upper mantle  
 981 depleted end-members lie along the  $\epsilon_{\text{Nd}}-\epsilon_{\text{Hf}}$  mantle array ( $[1.4 * \epsilon_{\text{Nd}}] + 2.8$ ), thereby deriving  $\epsilon_{\text{Hf}}$   
 982 from existing  $\epsilon_{\text{Nd}}$  values (Table 6). The poorly constrained  $\epsilon_{\text{Hf}}$  values for the Pan African  
 983 lithosphere end-member likely lie below the mantle array, and to estimate them we performed a  
 984 best-fit for Group 4b (this group extends to the least radiogenic values of  $\epsilon_{\text{Nd}}$  and  $\epsilon_{\text{Hf}}$ ). We then  
 985 derived  $\epsilon_{\text{Hf}}$  from where this best-fit line intersects the plane defined by the modeled  $\epsilon_{\text{Nd}}$  of the  
 986 Pan African lithosphere end-member.

989

990 References

991

- 992 Abbate, E., Azzaroli, A., Zanettin, B. and Visentin, E.J., 1968. A geologic and  
993 petrographic mission of the "Consiglio Nazionale delle Ricerche" to Ethiopia  
994 1967-1968 - Preliminary results. *Bollettino Società Geologica Italiana*, 87: 1-20.
- 995 Abbate, E. and Sagri, M., 1969. Datie considerazioni sul margine orientale dell'altopiano  
996 etiopico nell province del Tigray e del Wollo. *Bollettino Società Geologica Italiana*,  
997 88: 489-497.
- 998 Aitchison, J., 1986. *The statistical analysis of compositional data*. Chapman and Hall,  
999 London, New York.
- 1000 Antonellini, M.A. and Cambray, F.W., 1992. Relations between sill intrusions and  
1001 dedding-parallel extensional shear zones in the Midcontinent Rift System of the  
1002 Lake-Superior region. *Tectonophysics*, 212(3-4): 331-349.
- 1003 Ayalew, D., Barbey, P., Marty, B., Reisberg, L., Yirgu, G. and Pik, R., 2002. Source,  
1004 genesis, and timing of giant ignimbrite deposits associated with Ethiopian  
1005 continental flood basalts. *Geochimica et Cosmochimica Acta*, 66(8): 1429-1448.
- 1006 Ayalew, D. and Gibson, S.A., 2009. Head-to-tail transition of the Afar mantle plume:  
1007 Geochemical evidence from a Miocene bimodal basalt-rhyolite succession in the  
1008 Ethiopian Large Igneous Province. *Lithos*, 112(3-4): 461-476.
- 1009 Ayele, A., Stuart, G., Bastow, I. and Keir, D., 2007. The August 2002 earthquake  
1010 sequence in north Afar: Insights into the neotectonics of the Danakil microplate.  
1011 *Journal of African Earth Sciences*, 48(2-3): 70-79.
- 1012 Bachmann, O. and Bergantz, G.W., 2008. Rhyolites and their source mushes across  
1013 tectonic settings. *Journal of Petrology*, 49(12): 2277-2285.
- 1014 Baker, J., Snee, L. and Menzies, M., 1996a. A brief Oligocene period of flood volcanism  
1015 in Yemen: Implications for the duration and rate of continental flood volcanism at  
1016 the Afro-Arabian triple junction. *Earth and Planetary Science Letters*, 138(1-4):  
1017 39-55.
- 1018 Baker, J.A., Thirlwall, M.F. and Menzies, M.A., 1996b. Sr-Nd-Pb isotopic and trace  
1019 element evidence for crustal contamination of plume-derived flood basalts:  
1020 Oligocene flood volcanism in western Yemen. *Geochimica Et Cosmochimica*  
1021 *Acta*, 60(14): 2559-2581.
- 1022 Bastow, I.D. and Keir, D., 2011. The protracted development of the continent-ocean  
1023 transition in Afar. *Nature Geoscience*, 4(4): 248-250.
- 1024 Bastow, I.D., Nyblade, A.A., Stuart, G.W., Rooney, T.O. and Benoit, M.H., 2008. Rifting  
1025 at the edge of the African low velocity anomaly. *Geochemistry Geophysics*  
1026 *Geosystems*: Q12022, doi:10.1029/2008GC002107.
- 1027 Bastow, I.D., Pilidou, S., Kendall, J.M. and Stuart, G.W., 2010. Melt-Induced seismic  
1028 anisotropy and magma assisted rifting in Ethiopia: evidence from surface waves.  
1029 *Geochemistry Geophysics Geosystems*: Q0AB05, doi:10.1029/2010GC003036

- 1030 Beccaluva, L., Bianchini, G., Natali, C. and Siena, F., 2009. Continental flood basalts  
1031 and mantle plumes: a case study of the Northern Ethiopian Plateau. *Journal of*  
1032 *Petrology*, 50(7): 1377-1403.
- 1033 Behn, M.D., Buck, W.R. and Sacks, I.S., 2006. Topographic controls on dike injection in  
1034 volcanic rift zones. *Earth and Planetary Science Letters*, 246(3-4): 188-196.
- 1035 Berckhemer, H., Baier, B., Bartelsen, H., Behle, A., Burkhardt, H., Gebrande, H.,  
1036 Makris, J., Menzel, H., Miller, H. and Vees, R., 1975. Deep seismic soundings in  
1037 the Afar region and on the highland of Ethiopia. In: Pilger, A. and Roesler, A.  
1038 (Eds), *Afar between continental and oceanic rifting*. Schweizerbart, Stuttgart, 89-  
1039 107.
- 1040 Bialas, R.W., Buck, W.R. and Qin, R., 2010. How much magma is required to rift a  
1041 continent? *Earth and Planetary Science Letters*, 292: 68-78.
- 1042 Bilham, R., Bendick, R., Larson, K., Mohr, P., Braun, J., Tesfaye, S. and Asfaw, L.,  
1043 1999. Secular and tidal strain across the main Ethiopian rift. *Geophysical*  
1044 *Research Letters*, 26(18): 2789-2792.
- 1045 Bonini, M., Corti, G., Innocenti, F., Manetti, P., Mazzarini, F., Abebe, T. and Pecskey,  
1046 Z., 2005. Evolution of the Main Ethiopian Rift in the frame of Afar and Kenya rifts  
1047 propagation. *Tectonics*, 24(1): TC1007, doi: 10.1029/2004TC00168.
- 1048 Bonini, M., Sokoutis, D., Mulugeta, G., Boccaletti, M., Corti, G., Innocenti, F., Manetti, P.  
1049 and Mazzarini, F., 2001. Dynamics of magma emplacement in centrifuge models  
1050 of continental extension with implications for flank volcanism. *Tectonics*, 20(6):  
1051 1053-1065.
- 1052 Bosworth, W., Huchon, P. and McClay, K., 2005. The Red Sea and Gulf of Aden basins.  
1053 *Journal of African Earth Sciences*, 43(1-3): 334-378.
- 1054 Boynton, W.V., 1984. Cosmochemistry of the rare earth elements: meteorite studies. In:  
1055 Henderson, P. (Eds), *Rare earth element geochemistry*. Elsevier, New York.
- 1056 Buck, W.R., 2004. Consequences of asthenospheric variability on continental rifting. In:  
1057 Karner, G., Taylor, B., Driscoll, N.W. and Kohlstedt, D.L. (Eds), *Rheology and*  
1058 *deformation of the lithosphere at continental margins*. Columbia University Press,  
1059 New York, 1-30.
- 1060 Buck, W.R., 2006. The role of magma in the development of the Afro-Arabian rift  
1061 system. In: Yirgu, G., Ebinger, C. and Maguire, P. (Eds), *The Afar Volcanic*  
1062 *Province within the East African Rift System*. Special Publication of the  
1063 *Geological Society*, London, 43-54.
- 1064 Casey, M., Ebinger, C., Keir, D., Gloaguen, R. and Mohamed, F., 2006. Strain  
1065 accommodation in transitional rifts: Extension by magma intrusion and faulting in  
1066 Ethiopian rift magmatic segments. In: Yirgu, G., Ebinger, C. and Maguire, P.  
1067 (Eds), *The Afar Volcanic Province within the East African Rift System*. Geological  
1068 *Society*, London, London, 143-164.
- 1069 Catanzaro, E.J., Murphy, T.J., Shields, W.R. and Garner, E.L., 1968. Absolute isotopic  
1070 abundance ratios of common equal-atom and radiogenic lead isotopic standards.  
1071 *Journal of Research of the National Bureau of Standards: Section a-Physics and*  
1072 *Chemistry*, 72A(3): 26.
- 1073 Corti, G., 2009. Continental rift evolution: From rift initiation to incipient break-up in the  
1074 Main Ethiopian Rift, East Africa. *Earth-Science Reviews*, 96(1-2): 1-53.

- 1075 Daly, E., Keir, D., Ebinger, C.J., Stuart, G.W., Bastow, I.D. and Ayele, A., 2008. Crustal  
1076 tomographic imaging of a transitional continental rift: the Ethiopian rift.  
1077 *Geophysical Journal International*, 172(3): 1033-1048.
- 1078 Deering, C.D., Cole, J.W. and Vogel, T.A., 2008. A rhyolite compositional continuum  
1079 governed by lower crustal source conditions in the Taupo Volcanic Zone, New  
1080 Zealand. *Journal of Petrology*, 49(12): 2245-2276.
- 1081 Deniel, C., Vidal, P., Coulon, C. and Vellutini, P.J., 1994. Temporal evolution of mantle  
1082 sources during continental rifting - the volcanism of Djibouti (Afar). *Journal of*  
1083 *Geophysical Research-Solid Earth*, 99(B2): 2853-2869.
- 1084 Dugda, M.T., Nyblade, A.A. and Julia, J., 2007. Thin lithosphere beneath the Ethiopian  
1085 plateau revealed by a joint inversion of Rayleigh wave group velocities and  
1086 receiver functions. *Journal of Geophysical Research-Solid Earth*, 112(B8):  
1087 B08305, doi:10.1029/2006JB004918.
- 1088 Ebinger, C., Ayele, A., Keir, D., Rowland, J., Yirgu, G., Wright, T., Belachew, M. and  
1089 Hamling, I., 2010. Length and Timescales of Rift Faulting and Magma Intrusion:  
1090 The Afar Rifting Cycle from 2005 to Present. *Annual Review of Earth and*  
1091 *Planetary Sciences*, Vol 38, 38: 439-466.
- 1092 Ebinger, C.J. and Casey, M., 2001. Continental breakup in magmatic provinces: An  
1093 Ethiopian example. *Geology*, 29(6): 527-530.
- 1094 Ebinger, C.J. and Sleep, N.H., 1998. Cenozoic magmatism throughout East Africa  
1095 resulting from impact of a single plume. *Nature*, 395(6704): 788-791.
- 1096 Ellis, M. and King, G., 1991. Structural control of flank volcanism in continental rifts.  
1097 *Science*, 254(5033): 839-842.
- 1098 Fialko, Y.A. and Rubin, A.M., 1999. Thermal and mechanical aspects of magma  
1099 emplacement in giant dike swarms. *J. Geophys. Res.*, 104(B10): 23033-23049.
- 1100 Frey, H.M., Lange, R.A., Hall, C.M., Delgado-Granados, H. and Carmichael, I.S.E.,  
1101 2007. A Pliocene ignimbrite flare-up along the Tepic-Zacoalco rift: Evidence for  
1102 the initial stages of rifting between the Jalisco block (Mexico) and North America.  
1103 *Geological Society of America Bulletin*, 119(1-2): 49-64.
- 1104 Furman, T., Bryce, J.G., Karson, J. and Iotti, A., 2004. East African Rift System (EARS)  
1105 plume structure: Insights from quaternary mafic lavas of Turkana, Kenya. *Journal*  
1106 *of Petrology*, 45(5): 1069-1088.
- 1107 Furman, T., Bryce, J.G., Rooney, T., Hanan, B.B., Yirgu, G. and Ayalew, D., 2006.  
1108 Heads and tails: 30 million years of the Afar plume. In: Yirgu, G., Ebinger, C. and  
1109 Maguire, P. (Eds), *The Afar Volcanic Province within the East African Rift*  
1110 *System*. Special Publication of the Geological Society, London, 95-120.
- 1111 George, R.M. and Rogers, N.W., 2002. Plume dynamics beneath the African Plate  
1112 inferred from the geochemistry of the Tertiary basalts of southern Ethiopia.  
1113 *Contributions to Mineralogy and Petrology*, 144(3): 286-304.
- 1114 Gortani, M. and Bianchi, A., 1937. Osservazioni geologiche e petrografiche nella  
1115 regione di Harar (Africa Orientale Italiana). *Bollettino Società Geologica Italiana*,  
1116 56: 499-516.
- 1117 Gortani, M. and Bianchi, A., 1973. Itinerari geologici nella Danalia meridionale e sugli  
1118 altipiani Hararini Missione Geologica dell'AGIP nella Danalia Meridionale e sugli  
1119 Altipiani Hararini (1936-1938). *Accademia Nazionale Lincei, Roma*, 240.

- 1120 Hall, C.M. and Farrell, J.W., 1995. Laser Ar-40/Ar-39 ages of tephra from Indian-Ocean  
1121 deep-sea sediments - tie points for the astronomical and geomagnetic polarity  
1122 Time Scales. *Earth and Planetary Science Letters*, 133(3-4): 327-338.
- 1123 Hanan, B.B. and Graham, D.W., 1996. Lead and helium isotope evidence from oceanic  
1124 basalts for a common deep source of mantle plumes. *Science*, 272(5264): 991-  
1125 995.
- 1126 Hanghoj, K., Storey, M. and Stecher, O., 2003. An isotope and trace element study of  
1127 the East Greenland Tertiary dyke swarm: Constraints on temporal and spatial  
1128 evolution during continental rifting. *Journal of Petrology*, 44(11): 2081-2112.
- 1129 Hart, S.R., 1984. A large-scale isotope anomaly in the southern-hemisphere mantle.  
1130 *Nature*, 309(5971): 753-757.
- 1131 Hart, W.K., Woldegabriel, G., Walter, R.C. and Mertzman, S.A., 1989. Basaltic  
1132 volcanism in Ethiopia - Constraints on continental rifting and mantle interactions.  
1133 *Journal of Geophysical Research-Solid Earth and Planets*, 94(B6): 7731-7748.
- 1134 Herzberg, C., 2011. Identification of Source Lithology in the Hawaiian and Canary  
1135 Islands: Implications for Origins. *Journal of Petrology*, 52(1): 113-146.
- 1136 Hofmann, C., Courtillot, V., Feraud, G., Rouchett, P., Yirgu, G., Ketefo, E. and Pik, R.,  
1137 1997. Timing of the Ethiopian flood basalt event and implications for plume birth  
1138 and global change. *Nature*, 389(6653): 838-841.
- 1139 Huismans, R.S., Podladchikov, Y.Y. and Cloetingh, S., 2001. Transition from passive to  
1140 active rifting: Relative importance of asthenospheric doming and passive  
1141 extension of the lithosphere. *Journal of Geophysical Research-Solid Earth*,  
1142 106(B6): 11271-11291.
- 1143 Hyodo, H. and York, D., 1993. The discovery and significance of a fossilized radiogenic  
1144 argon wave (Argonami) in the Earth's crust. *Geophysical Research Letters*,  
1145 20(1): 61-64.
- 1146 Jellinek, A.M. and DePaolo, D.J., 2003. A model for the origin of large silicic magma  
1147 chambers: precursors of caldera-forming eruptions. *Bulletin of Volcanology*,  
1148 65(5): 363-381.
- 1149 Jepsen, D.H. and Athearn, M.J., 1962. East-west geologic sections, Blue Nile river  
1150 basin, Ethiopia. Dept. of Water Resources, Addis Ababa, Drawing No. 5.2 BN-3.
- 1151 Justin-Visentin, E. and Zanettin, B., 1974. Dike swarms, volcanism and tectonics of the  
1152 Western Afar margin along the Kombolcha-Eloa traverse (Ethiopia). *Bulletin of*  
1153 *Volcanology*, 38: 187-205.
- 1154 Kazmin, V., Berhe, S.M. and Wondm-Agennehu, B., 1981. Geological map of the  
1155 Ethiopian Rift. The Ethiopian Government - Ministry of Mines, Energy and Water  
1156 Resources, Addis Ababa.
- 1157 Keir, D., Belachew, M., Ebinger, C.J., Kendall, J.M., Hammond, J.O.S., Stuart, G.W.,  
1158 Ayele, A. and Rowland, J.V., 2011a. Mapping the evolving strain field during  
1159 continental breakup from crustal anisotropy in the Afar Depression. *Nature*  
1160 *Communications*, 2.
- 1161 Keir, D., Hamling, I.J., Ayele, A., Calais, E., Ebinger, C., Wright, T.J., Jacques, E.,  
1162 Mohamed, K., Hammond, J.O.S., Belachew, M., Baker, E., Rowland, J.V., Lewi,  
1163 E. and Bennati, L., 2009. Evidence for focused magmatic accretion at segment  
1164 centers from lateral dike injections captured beneath the Red Sea rift in Afar.  
1165 *Geology*, 37(1): 59-62.

- 1166 Keir, D., Pagli, C., Bastow, I.D. and Ayele, A., 2011b. The magma-assisted removal of  
1167 Arabia in Afar: Evidence from dike injection in the Ethiopian rift captured using  
1168 InSAR and seismicity. *Tectonics*, 30.
- 1169 Keranen, K., Klemperer, S.L., Gloaguen, R., Asfaw, L., Ayele, A., Ebinger, C., Furman,  
1170 T., Harder, S., Keller, G.R., Mackenzie, G.D., Maguire, P.K.H. and Stuart, G.W.,  
1171 2004. Three-dimensional seismic imaging of a protoridge axis in the main  
1172 Ethiopian Rift. *Geology*, 32(11): 949-952.
- 1173 Kieffer, B., Arndt, N., Lapierre, H., Bastien, F., Bosch, D., Pecher, A., Yirgu, G., Ayalew,  
1174 D., Weis, D., Jerram, D.A., Keller, F. and Meugniot, C., 2004. Flood and shield  
1175 basalts from Ethiopia: Magmas from the African superswell. *Journal of Petrology*,  
1176 45(4): 793-834.
- 1177 Klausen, M. and Larsen, H., 2002. East Greenland coast-parallel dike swarm and its  
1178 role in continental breakup. In: Menzies, M., Klemper, S.L., Ebinger, C.J. and  
1179 Baker, J. (Eds), *Volcanic Rifted Margins*. Geological Society of America, Boulder,  
1180 Co, 133-158.
- 1181 Leroy, S., d'Acremont, E., Tiberi, C., Basuyau, C., Autin, J., Lucazeau, F. and Sloan, H.,  
1182 2010. Recent off-axis volcanism in the eastern Gulf of Aden: Implications for  
1183 plume-ridge interaction. *Earth and Planetary Science Letters*, 293: 140-153.
- 1184 Maguire, P., Keller, G.R., Klemper, S.L., Mackenzie, G., Keranen, K., Harder, S.,  
1185 O'Reilly, B., Thybo, H., Asfaw, L., Kahn, M. and Amha, M., 2006. Crustal  
1186 structure of the Northern Main Ethiopian Rift from the EAGLE controlled source  
1187 survey; a snapshot of incipient lithospheric break-up. In: Yirgu, G., Ebinger, C.  
1188 and Maguire, P. (Eds), *The Afar Volcanic Province within the East African Rift  
1189 System*. Special Publication of the Geological Society, London, 269-292.
- 1190 Manhes, G., Minster, J.F. and Allegre, C.J., 1978. Comparative uranium-thorium-lead  
1191 and rubidium-strontium study of Saint-Severin amphoterite - consequences for  
1192 early Solar-System chronology. *Earth and Planetary Science Letters*, 39(1): 14-  
1193 24.
- 1194 Marty, B., Pik, R. and Gezahegn, Y., 1996. Helium isotopic variations in Ethiopian  
1195 plume lavas; nature of magmatic sources and limit on lower mantle contribution.  
1196 *Earth and Planetary Science Letters*, 144(1-2): 223-237.
- 1197 Megrue, G.H., Norton, E. and Strangway, D.W., 1972. Tectonic history of Ethiopian Rift  
1198 as deduced by K-Ar ages and paleomagnetic measurements of basaltic dikes.  
1199 *Journal of Geophysical Research*, 77(29): 5744-5754.
- 1200 Meshesha, D., and Shinjo, R., 2007, Crustal contamination and diversity of magma  
1201 sources in the northwestern Ethiopian volcanic province: *Journal of Mineralogical  
1202 and Petrological Sciences*, v. 102, p. 272-290.
- 1203 Meshesha, D., and Shinjo, R., 2010, Hafnium isotope variations in Bure volcanic rocks  
1204 from the northwestern Ethiopian volcanic province: a new insight for mantle  
1205 source diversity: *Journal of Mineralogical and Petrological Sciences*, v. 105, p.  
1206 101-111.
- 1207 Mohr, P., 1971. Ethiopian Tertiary dike swarms, 339. Smithsonian Institution, Research  
1208 in Space Science, SAO Special Report 339.
- 1209 Mohr, P., 1978. Afar. *Annual Review of Earth and Planetary Sciences*, 6: 145-172.
- 1210 Mohr, P., 1983a. Ethiopian flood basalt province. *Nature*, 303(5918): 577-584.

- 1211 Mohr, P., 1983b. The Morton-Black hypothesis for the thinning of continental-crust  
1212 revisited in western Afar. *Tectonophysics*, 94(1-4): 509-528.
- 1213 Mohr, P., 1999. The Asmara dike swarm, Eritrean Plateau; physical parameters of an  
1214 off-rift olivine dolerite injection zone. *Acta Vulcanologica*, 11(1): 177-181.
- 1215 Mohr, P.A., 1962. The Ethiopian rift system. *Bulletin of the Geophysical Observatory*,  
1216 3(1): 33-62.
- 1217 Morton, W.H. and Black, R., 1975. Crustal attenuation in Afar. In: Pilger, A. and Rosler,  
1218 A. (Eds), *Afar Depression of Ethiopia*. Schweizerbart, Stuttgart, 55-65.
- 1219 Morton, W.H., Rex, D.C., Mitchell, J.G. and Mohr, P., 1979. Riftward younging of  
1220 volcanic units in the Addis Ababa region, Ethiopian Rift valley. *Nature*,  
1221 280(5720): 284-288.
- 1222 Myers, J.S., 1980. Structure of the coastal dyke swarm and associated plutonic  
1223 intrusions of East Greenland. *Earth and Planetary Science Letters*, 46(3): 407-  
1224 418.
- 1225 Peate, D.W., Barker, A.K., Riishuus, M.S. and Andreassen, R., 2008. Temporal  
1226 variations in crustal assimilation of magma suites in the East Greenland flood  
1227 basalt province: Tracking the evolution of magmatic plumbing systems. *Lithos*,  
1228 102(1-2): 179-197.
- 1229 Peccerillo, A., Barberio, M.R., Yirgu, G., Ayalew, D., Barbieri, M. and Wu, T.W., 2003.  
1230 Relationships between mafic and peralkaline silicic magmatism in continental rift  
1231 settings: A petrological, geochemical and isotopic study of the Gedemsa volcano,  
1232 central Ethiopian rift. *Journal of Petrology*, 44(11): 2003-2032.
- 1233 Peccerillo, A., Donati, C., Santo, A.P., Orlando, A., Yirgu, G. and Ayalew, D., 2007.  
1234 Petrogenesis of silicic peralkaline rocks in the Ethiopian rift: Geochemical  
1235 evidence and volcanological implications. *Journal of African Earth Sciences*,  
1236 48(2-3): 161-173.
- 1237 Pik, R., Deniel, C., Coulon, C., Yirgu, G., Hofmann, C. and Ayalew, D., 1998. The  
1238 northwestern Ethiopian Plateau flood basalts. Classification and spatial  
1239 distribution of magma types. *Journal of Volcanology and Geothermal Research*,  
1240 81(1-2): 91-111.
- 1241 Pik, R., Deniel, C., Coulon, C., Yirgu, G. and Marty, B., 1999. Isotopic and trace element  
1242 signatures of Ethiopian flood basalts; evidence for plume-lithosphere interactions.  
1243 *Geochimica et Cosmochimica Acta*, 63(15): 2263-2279.
- 1244 Renne, P.R., Deckart, K., Ernesto, M., Fe´raud, G. and Piccirillo, E.M., 1996. Age of the  
1245 Ponta Grossa dike swarm (Brazil), and implications to Parana´ flood volcanism.  
1246 *Earth and Planetary Science Letters*, 144(1-2): 199-211.
- 1247 Rooney, T., Furman, T., Bastow, I.D., Ayalew, D. and Gezahegn, Y., 2007. Lithospheric  
1248 modification during crustal extension in the Main Ethiopian Rift. *Journal of*  
1249 *Geophysical Research, B, Solid Earth and Planets*, 112: B10201,  
1250 doi:10.1029/2006JB004916.
- 1251 Rooney, T., Furman, T., Yirgu, G. and Ayalew, D., 2005. Structure of the Ethiopian  
1252 lithosphere: Xenolith evidence in the Main Ethiopian Rift. *Geochimica et*  
1253 *Cosmochimica Acta*, 69(15): 3889-3910.
- 1254 Rooney, T.O., 2010. Geochemical evidence of lithospheric thinning in the southern Main  
1255 Ethiopian Rift. *Lithos*, 117(1-4): 33-48.



- 1256 Rooney, T.O., Bastow, I.D. and Keir, D., 2011. Insights into extensional processes  
1257 during magma assisted rifting: evidence from aligned scoria cones and maars  
1258 *Journal of Volcanology and Geothermal Research*, 201(1-4): 83-96.
- 1259 Rooney, T.O., Hanan, B.B., Graham, D.W., Furman, T., Blichert-Toft, J. and Schilling,  
1260 J.-G., 2012a. Upper Mantle Pollution during Afar Plume–Continental Rift  
1261 Interaction. *Journal of Petrology*, 53: 365-389.
- 1262 Rooney, T.O., Hart, W.K., Hall, C.M., Ayalew, D., Ghiorso, M.S., Hidalgo, P. and Yirgu,  
1263 G., 2012b. Peralkaline magma evolution and the tephra record in the Ethiopian  
1264 Rift *Contributions to Mineralogy and Petrology*, DOI: 10.1007/s00410-012-0744-  
1265 6.
- 1266 Rooney, T.O., Herzberg, C. and Bastow, I.D., 2012c. Elevated mantle temperature  
1267 beneath East Africa. *Geology*, 40(1): 27-30.
- 1268 Samson, S.D. and Alexander, E.C., 1987. Calibration of the interlaboratory Ar-40 Ar-39  
1269 dating standard, Mmhb-1. *Chemical Geology*, 66(1-2): 27-34.
- 1270 Schilling, J.G., 1973. Afar Mantle Plume - rare-earth evidence. *Nature-Physical Science*,  
1271 242(114): 2-5.
- 1272 Schilling, J.G., Kingsley, R.H., Hanan, B.B. and McCully, B.L., 1992. Nd-Sr-Pb isotopic  
1273 variations along the Gulf of Aden - Evidence for Afar mantle plume continental  
1274 lithosphere interaction. *Journal of Geophysical Research-Solid Earth*, 97(B7):  
1275 10927-10966.
- 1276 Schultz, R.A., Soliva, R., Fossen, H., Okubo, C.H. and Reeves, D.M., 2008.  
1277 Dependence of displacement-length scaling relations for fractures and  
1278 deformation bands on the volumetric changes across them. *Journal of Structural*  
1279 *Geology*, 30(11): 1405-1411.
- 1280 Sleep, N.H., 2008. Channeling at the base of the lithosphere during the lateral flow of  
1281 plume material beneath flow line hot spots. *Geochemistry Geophysics*  
1282 *Geosystems*, 9: Q08005, doi:10.1029/2008GC002090.
- 1283 Sobolev, A.V., Hofmann, A.W., Kuzmin, D.V., Yaxley, G.M., Arndt, N.T., Chung, S.L.,  
1284 Danyushevsky, L.V., Elliott, T., Frey, F.A., Garcia, M.O., Gurenko, A.A.,  
1285 Kamenetsky, V.S., Kerr, A.C., Krivolutsкая, N.A., Matvienkov, V.V., Nikogosian,  
1286 I.K., Rocholl, A., Sigurdsson, I.A., Sushchevskaya, N.M. and Teklay, M., 2007.  
1287 The amount of recycled crust in sources of mantle-derived melts. *Science*,  
1288 316(5823): 412-417.
- 1289 Sobolev, A.V., Hofmann, A.W., Sobolev, S.V. and Nikogosian, I.K., 2005. An olivine-free  
1290 mantle source of Hawaiian shield basalts. *Nature*, 434(7033): 590-597.
- 1291 Stewart, K. and Rogers, N., 1996. Mantle plume and lithosphere contributions to basalts  
1292 from southern Ethiopia. *Earth and Planetary Science Letters*, 139(1-2): 195-211.
- 1293 Sun, S.s.-. and McDonough, W.F., 1989. Chemical and isotopic systematics of oceanic  
1294 basalts: Implications for mantle composition and processes. In: Saunders, A.D.  
1295 (Eds), *Magmatism in the ocean basins*. Geological Society, London, 313 - 345.
- 1296 Tanaka, T., Togashi, S., Kamioka, H., Amakawa, H., Kagami, H., Hamamoto, T.,  
1297 Yuhara, M., Orihashi, Y., Yoneda, S., Shimizu, H., Kunimaru, T., Takahashi, K.,  
1298 Yanagi, T., Nakano, T., Fujimaki, H., Shinjo, R., Asahara, Y., Tanimizu, M. and  
1299 Dragusanu, C., 2000. JNdi-1: a neodymium isotopic reference in consistency  
1300 with LaJolla neodymium. *Chemical Geology*, 168(3-4): 279-281.

- 1301 Tegner, C., Leshner, C.E., Larsen, L.M. and Watt, W.S., 1998. Evidence from the rare-  
1302 earth-element record of mantle melting for cooling of the tertiary Iceland plume.  
1303 *Nature*, 395(6702): 591-594.
- 1304 Tilton, G.R., 1973. Isotopic lead ages of chondritic meteorites. *Earth and Planetary*  
1305 *Science Letters*, 19(3): 321-329.
- 1306 Trua, T., Deniel, C. and Mazzuoli, R., 1999. Crustal control in the genesis of Plio-  
1307 Quaternary bimodal magmatism of the Main Ethiopian Rift (MER); geochemical  
1308 and isotopic (Sr, Nd, Pb) evidence. *Chemical Geology*, 155(3-4): 201-231.
- 1309 Turner, G. and Cadogan, P.H., 1974. Possible effects of  $^{39}\text{Ar}$  recoil in  $^{40}\text{Ar}$  dating. ,  
1310 *Proceedings of the Fifth Lunar Science Conference*, 1601-1615.
- 1311 Turner, G., Enright, M.C. and Cadogan, P.H., 1978. The early history of chondrite  
1312 parent bodies inferred from  $^{40}\text{Ar}$ - $^{39}\text{Ar}$  ages, *Proceedings of the Lunar and*  
1313 *Planetary Science Conference*, 989-1025.
- 1314 Ukstins, I.A., Renne, P.R., Wolfenden, E., Baker, J., Ayalew, D. and Menzies, M., 2002.  
1315 Matching conjugate volcanic rifted margins;  $^{40}\text{Ar}/^{39}\text{Ar}$  chrono-stratigraphy of  
1316 pre- and syn-rift bimodal flood volcanism in Ethiopia and Yemen. *Earth and*  
1317 *Planetary Science Letters*, 198(3-4): 289-306.
- 1318 van Wijk, J., van Hunen, J. and Goes, S., 2008. Small-scale convection during  
1319 continental rifting: Evidence from the Rio Grande rift. *Geology*, 36(7): 575-578.
- 1320 Vogel, T.A., Flood, T.P., Patino, L.C., Wilmot, M.S., Maximo, R.P.R., Arpa, C.B., Arcilla,  
1321 C.A. and Stimac, J.A., 2006. Geochemistry of silicic magmas in the Macolod  
1322 Corridor, SW Luzon, Philippines: evidence of distinct, mantle-derived, crustal  
1323 sources for silicic magmas. *Contributions to Mineralogy and Petrology*, 151(3):  
1324 267-281.
- 1325 Walker, G.P.L., 1960. Zeolite zones and dike distribution in relation to the structure of  
1326 the basalts of Eastern Iceland. *Journal of Geology*, 68(5): 515-528.
- 1327 Walter, R.C., 1980. The volcanic history of the Hadar early-man site and the  
1328 surrounding Afar region of Ethiopia, Ph.D., Case Western Reserve University,  
1329 426 pp.
- 1330 Wang, K., Plank, T., Walker, J.D. and Smith, E.I., 2002. A mantle melting profile across  
1331 the basin and range, SW USA. *Journal of Geophysical Research-Solid Earth*,  
1332 107(B1): 2017, doi:10.1029/2001JB0002092.
- 1333 White, R. and McKenzie, D., 1989. Magmatism at rift zones - the generation of volcanic  
1334 continental margins and flood basalts. *Journal of Geophysical Research-Solid*  
1335 *Earth and Planets*, 94(B6): 7685-7729.
- 1336 Wolfenden, E., Ebinger, C., Yirgu, G., Renne, P.R. and Kelley, S.P., 2005. Evolution of  
1337 a volcanic rifted margin: Southern Red Sea, Ethiopia. *Geological Society of*  
1338 *America Bulletin*, 117(7-8): 846-864.
- 1339 Wright, T.J., Sigmundsson, C.P., C., Belachew, M., Hamling, I., Brandsdottir, B., Keir,  
1340 D., Pedersen, R., Ayele, A., Ebinger, C., Einarsson, P., Lewi, E. and Calais, E.,  
1341 2012. Geophysical constraints on the dynamics of spreading centres from 1  
1342 rifting episodes on land. *Nature Geoscience*, In Press.
- 1343 Zanettin, B., 1992. Evolution of the Ethiopian Volcanic Province. *Memorie Lincee*  
1344 *Scienze Fisiche e Naturali*, 1: 155-181.
- 1345

**Table 1**

Unit	Composition	Basin	Age	Dike Group
Dahla Series <i>unconformity</i>	Fissure Basalts	3	c. 7-5 Ma*	3
Burka Formation <i>unconformity</i>	Basalts, rhyolites	2	c. 20-13 Ma	4a
Dese Formation <i>unconformity</i>	Basalts	1	c. 29.5-24 Ma	1, 4b
Ashangi, Aiba, Alaji	Flood basalts, rhyolites	throughout	c. 31.5-29.5**	2

\* Renne et al., (1999)  
\*\* Hofmann et al., (1997)

Table 1.

Table 2

Sector	-----Dikes-----		-----Faults-----	
	Strike	Dip	Strike	Dip
Desse-Combolcia:	N000-010°	W	N350-000°	W, E
	N060°	near-vertical	N065-080°*	NW
Combolcia-Batie:	N330-350°	W	N335-350°	W, E
	N020-030°	W	N020-040°	NW
	N045-060°	NW,SE	N040-075°	NW
	N300°	SW		
Batie-Eloa:	N330-350°	W	N340-350°	**
	N000-010°	W	N005-030°	W
	N050-060°	near-vertical	N060-080°	NW

\* This fault trend coincides with the axes of numerous small, gentle folds in the stratoid lavas.

\*\* The NNW-trending faults of the Batie-Eloa sector dip predominantly W (with E upthrows), but in the easternmost, Eloa zone the slip planes dip E.

Table 2

Table 3

Sample	Run	TGA (Ma)	+/-	RIA (Ma)	+/-	EWP (Ma)	+/-	CIA (Ma)	+/-	Preferred (Ma)	+/-	Megrue K-Ar (Ma)	+/-
EAD-111	a	24.67	0.25	24.67	0.25	24.27	0.17						
	b	23.89	0.21	23.95	0.18	23.56	0.16						
	Avg.	24.20	0.39	24.21	0.34	23.90	0.36	23.57	0.17	<b>23.57</b>	0.17	23.9	2.0
EAD-114	a	24.43	0.06	24.76	0.06	NA	-						
	b	24.58	0.08	24.77	0.08	NA	-						
	Avg.	24.48	0.07	24.76	0.05	-	-	24.82	0.13	<b>24.76</b>	0.05	23.1	0.9
EKA-112B	a	31.02	0.26	30.74	0.21	30.80	0.18						
	b	31.02	0.33	31.14	0.29	30.72	0.21						
	Avg.	31.02	0.20	30.88	0.19	30.77	0.14	30.75	0.16	<b>30.77</b>	0.14	NA	NA
EKA-116	a	28.56	0.34	29.85	0.21	29.79	0.19						
	b	28.94	0.41	29.36	0.37	29.14	0.28						
	c	28.65	0.30	28.87	0.24	29.79	0.22						
	Avg.	28.58	0.20	29.78	0.15	29.66	0.19	30.01	0.16	<b>29.78</b>	0.15	35.2	1.4
EKA-119	a	13.95	0.49	11.97	0.48	12.10	0.51						
	b	15.12	0.44	14.34	0.31	14.71	0.53						
	c	12.72	0.28	12.72	0.28	12.79	0.23						
	Avg.	13.51	0.71	13.20	0.65	12.95	0.53	12.51	0.33	<b>12.51</b>	0.33	15.7	1.1
EKA-120	a	27.69	0.34	27.96	0.32	NA							
	b	28.05	0.46	28.29	0.43	25.96	0.51						
	c	26.71	0.21	26.90	0.21	26.15	0.29						
	Avg.	27.13	0.39	27.37	0.41	26.10	0.26	28.02	0.27	<b>27.37</b>	0.41	31.8	1.4
EKA-140A	a	8.00	0.10	8.03	0.09	NA	-						
	b	8.61	0.11	8.72	0.11	9.21	0.12						
	Avg.	8.26	0.30	8.31	0.34	-	-	8.18	0.30	<b>8.31</b>	0.34	19.6	1.1
EKA-153	a	18.67	0.07	20.47	0.09	NA	-						
	b	19.83	0.07	20.59	0.06	NA	-						
	Avg.	19.34	0.57	20.55	0.06	-	-	21.23	0.36	<b>20.55</b>	0.06	NA	NA

Table 3.

Table 4

Sample	$^{87}\text{Sr}/^{86}\text{Sr}$	$2\sigma$	$^{143}\text{Nd}/^{144}\text{Nd}$	$2\sigma$	$^{206}\text{Pb}/^{204}\text{Pb}$	$2\sigma$	$^{207}\text{Pb}/^{204}\text{Pb}$	$2\sigma$	$^{208}\text{Pb}/^{204}\text{Pb}$	$2\sigma$	$^{176}\text{Hf}/^{177}\text{Hf}$	$2\sigma$
EKA-116	0.704713	9	0.512710	7	18.9293	9	15.6445	9	39.0598	26	0.282983	10
EKA-120	0.704722	8	0.512686	4	19.1851	13	15.6450	12	39.3051	35	0.282898	14
EKA-112B	0.704745	8	0.512781	6	18.2061	10	15.5638	9	38.4707	28	0.282995	13
EKA-140A	0.703647	6	0.512932	5	18.2683	12	15.5452	12	38.5000	34	0.283088	9
EKA-142	0.703449	10	0.512950	5	18.2285	10	15.5337	10	38.4161	24	0.283089	10
EKA-106	0.704443	8	0.512735	5	17.9460	8	15.5449	10	38.3195	30	0.282904	8
EKA-153	0.705482	10	0.512709	6	18.0249	11	15.5863	11	38.5694	30	0.282893	9
EKA-119	0.704333	8	0.512827	6	18.5287	10	15.5897	10	38.9792	33	0.282994	8
EAD-111	0.704514	8	0.512845	4	18.8366	12	15.6562	12	39.2479	34	0.283011	11
EAD-113	0.704286	9	0.512906	6	18.9878	9	15.6600	10	39.3444	30	0.283043	8
EAD-116	0.704101	12	0.512915	4	19.3556	10	15.6960	10	39.6695	27	0.283060	10
EAD-114	0.706728	8	0.512589	7	18.2142	8	15.6332	8	38.9070	22	0.282769	8

Table 4.

**Table 5**

Element	PC1	PC2	PC3
La	0.27	-0.30	0.15
Ce	0.30	-0.18	0.21
Pr	0.31	-0.14	0.06
Nd	0.32	0.00	0.03
Sm	0.29	0.24	0.10
Eu	0.23	0.36	-0.75
Gd	0.15	0.53	-0.04
Tb	-0.08	0.56	0.55
Dy	-0.29	0.23	0.06
Ho	-0.32	0.05	0.02
Er	-0.32	-0.04	0.01
Yb	-0.31	-0.09	-0.17
Lu	-0.31	-0.12	-0.10

Table 5

**Table 6**

End member	$\epsilon_{\text{Nd}}$	$\epsilon_{\text{Hf}}$	$^{87}\text{Sr}/^{86}\text{Sr}$	$^{206}\text{Pb}/^{204}\text{Pb}$	$^{207}\text{Pb}/^{204}\text{Pb}$	$^{208}\text{Pb}/^{204}\text{Pb}$
Pan African Lithosphere	-10.49	-15.35	0.7075	17.85	15.75	39.75
Depleted Mantle	13.89	22.24	0.7022	17.5	15.3	36.6
Afar Plume	4.62	9.27	0.7035	19.5	15.6	39.2

Table 6



Figure 1

Figure 1

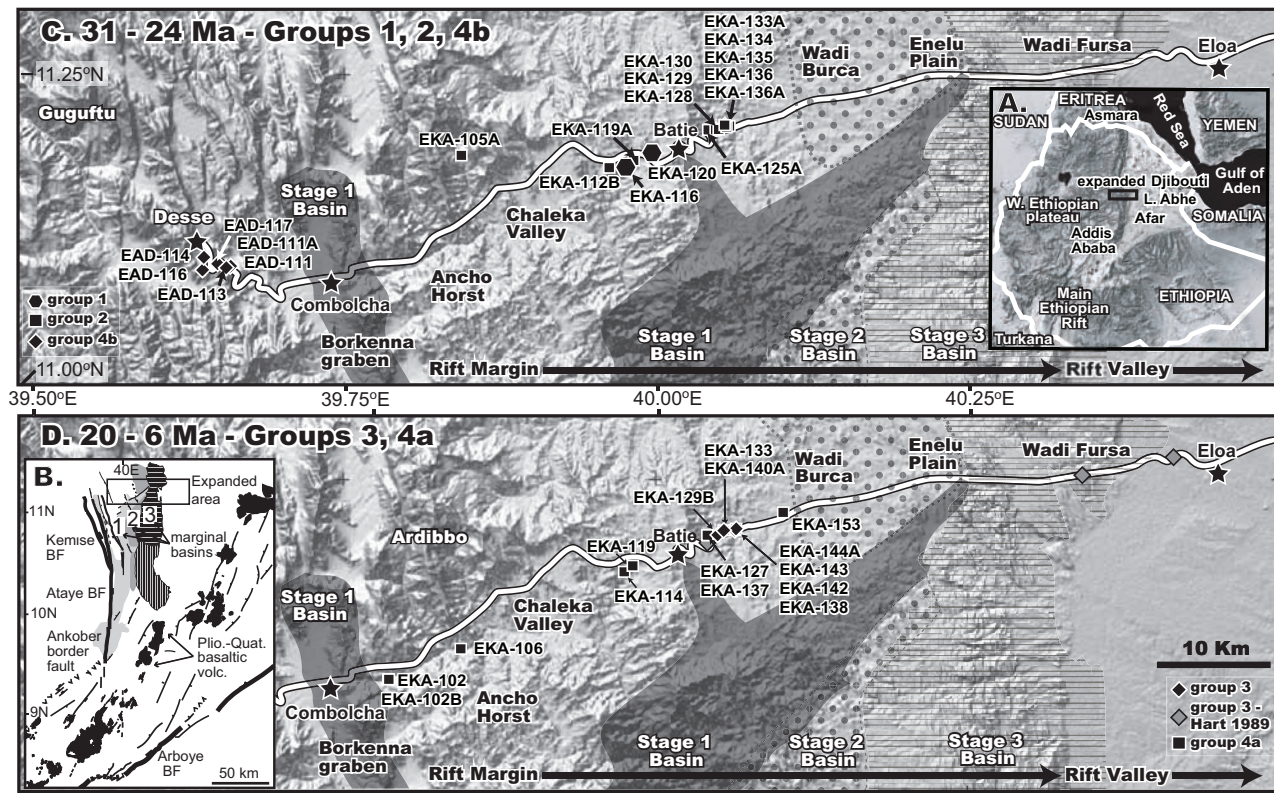
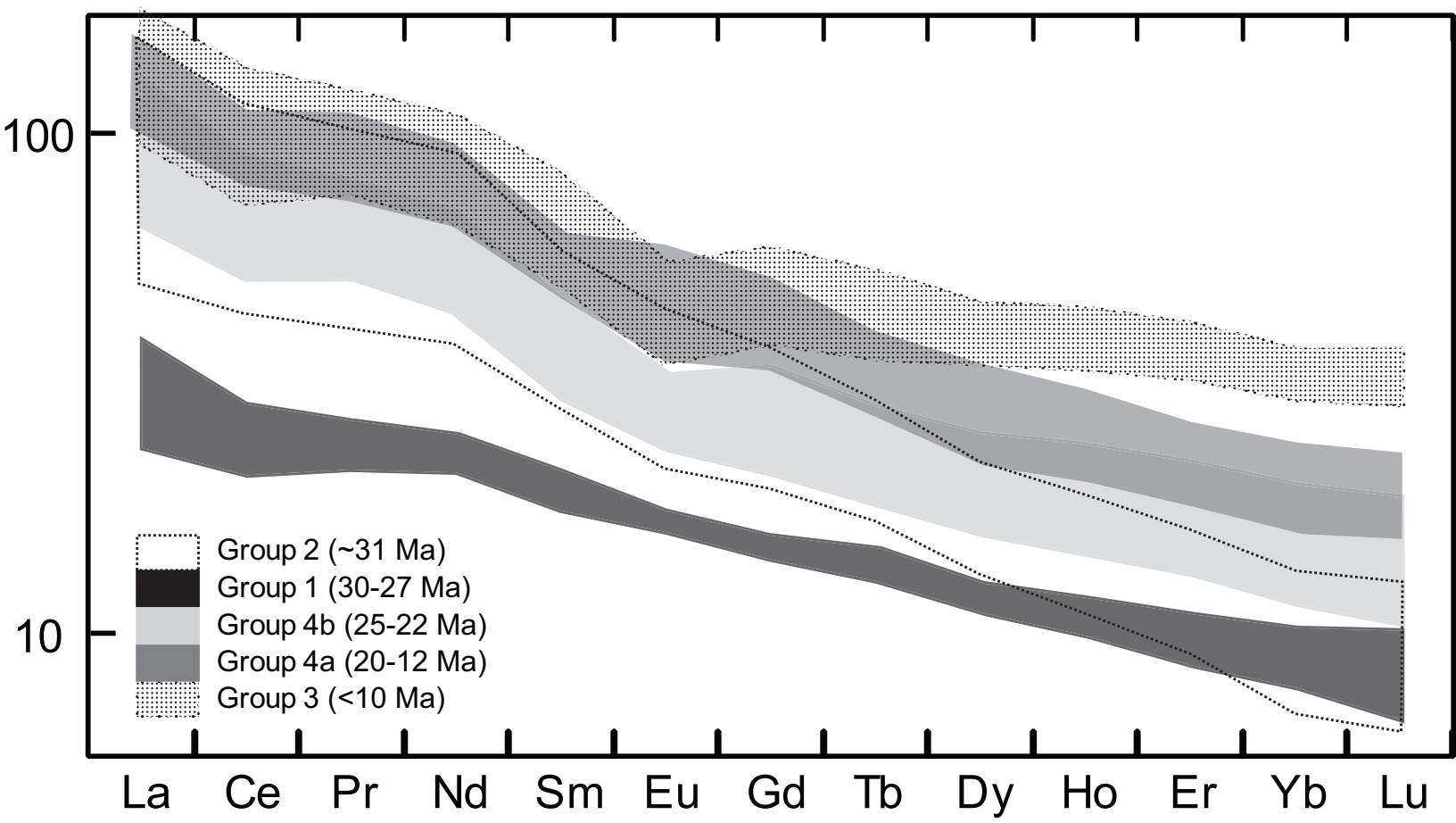


Figure 2



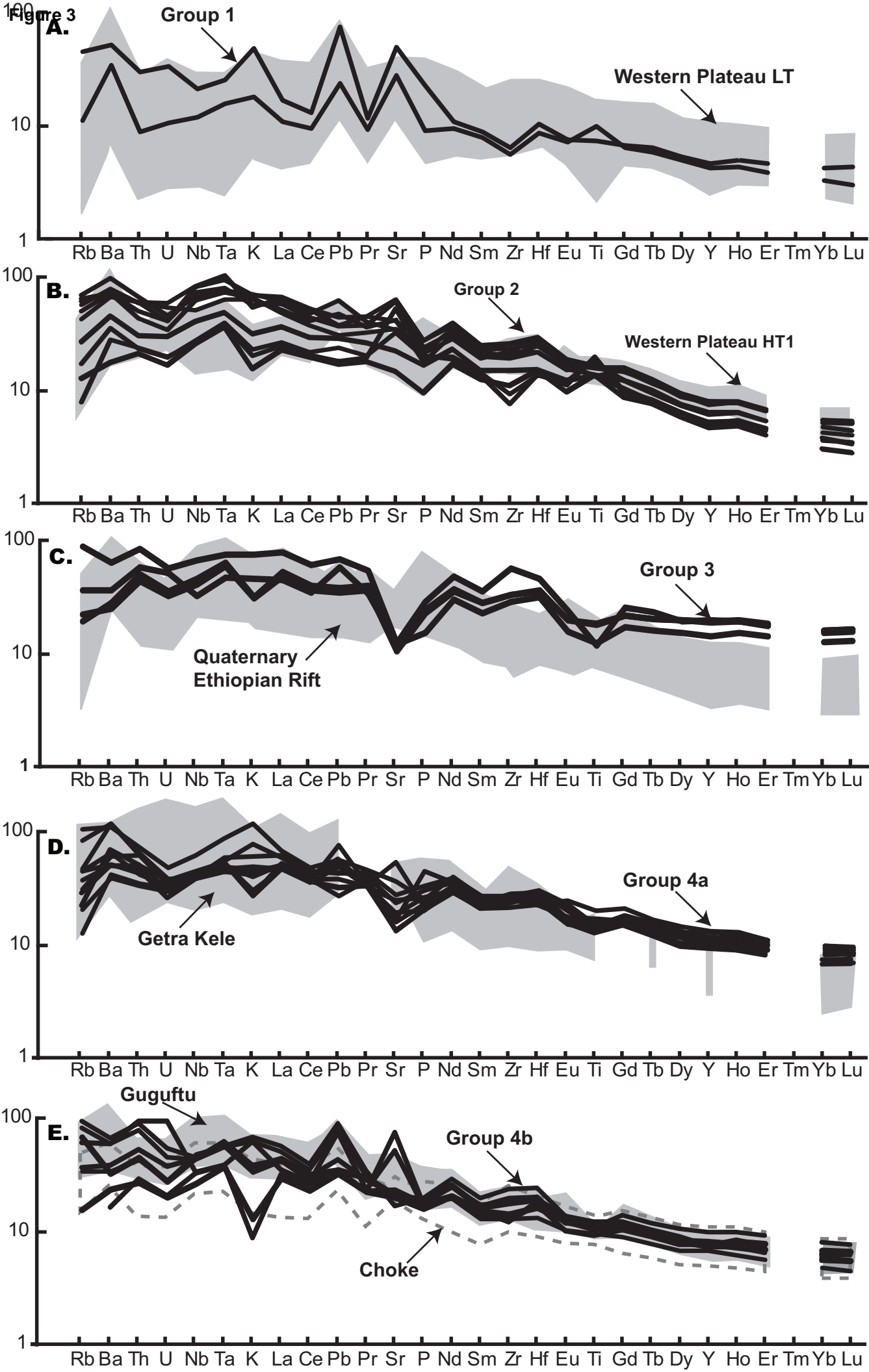
**Figure 3**

Figure 4a

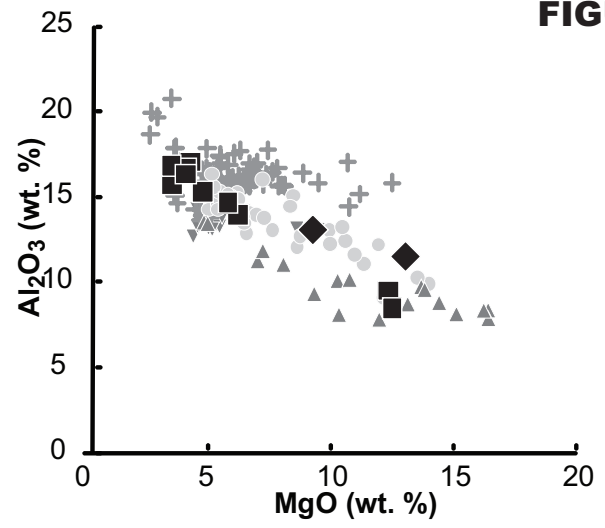
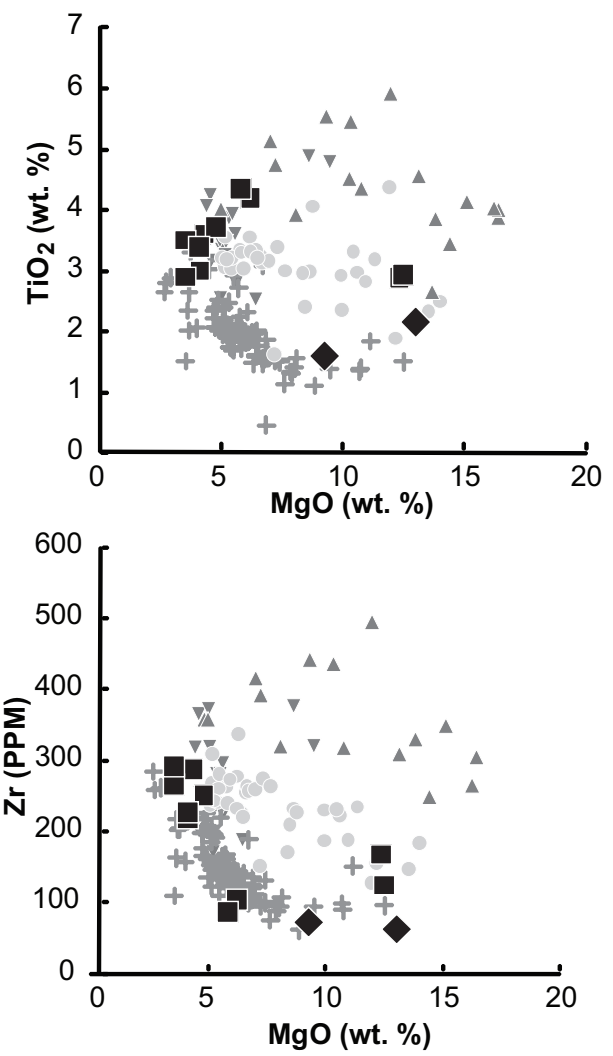


FIGURE 4A

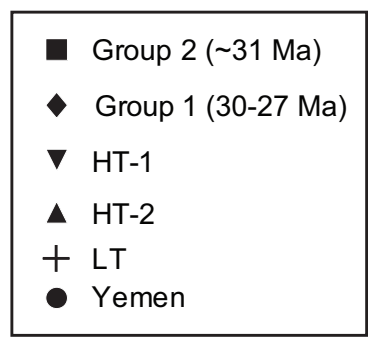
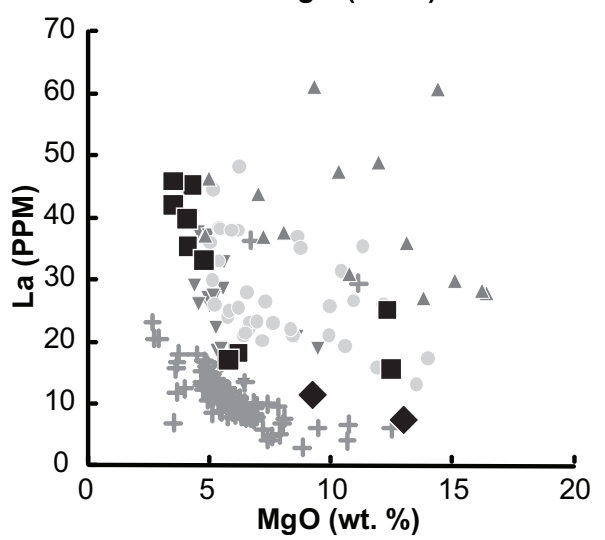
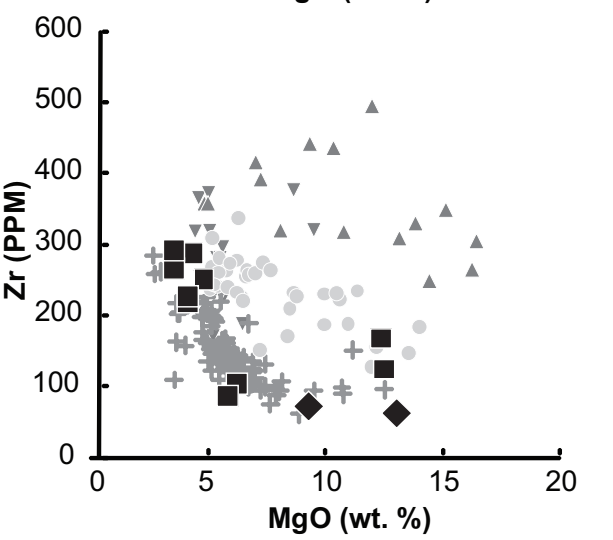


Figure 4b

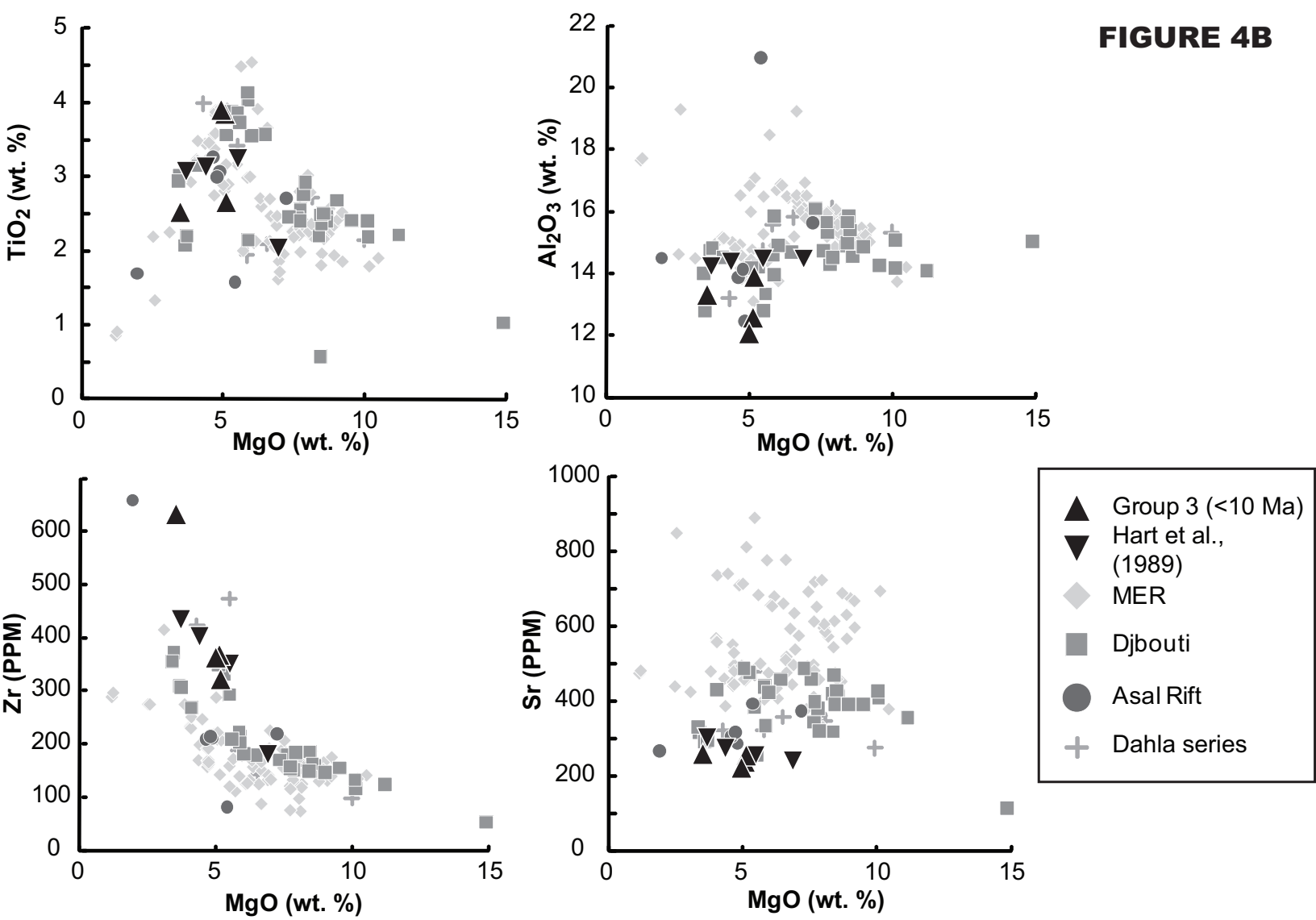


FIGURE 4B

Figure 4c

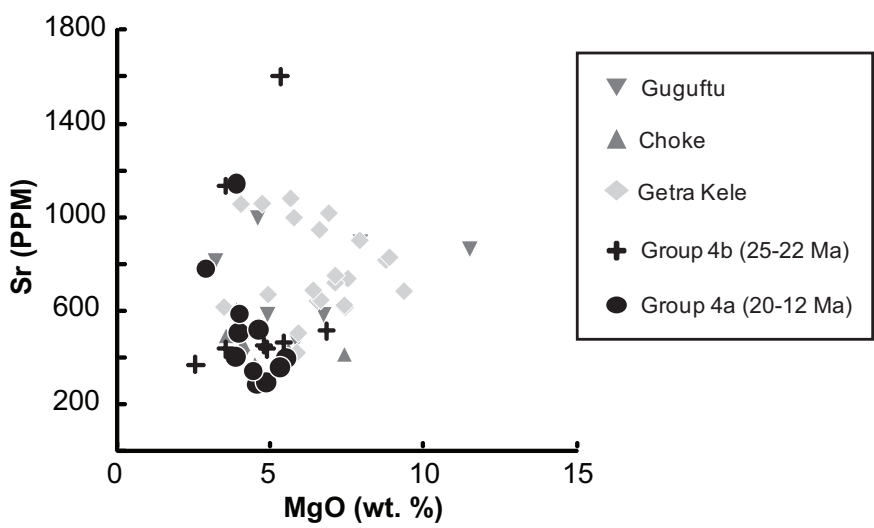
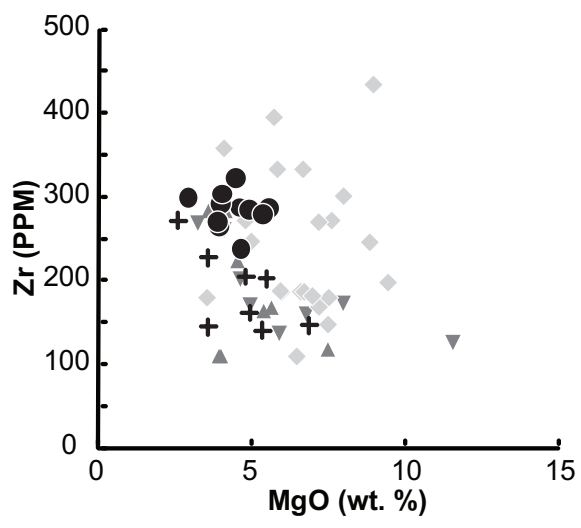
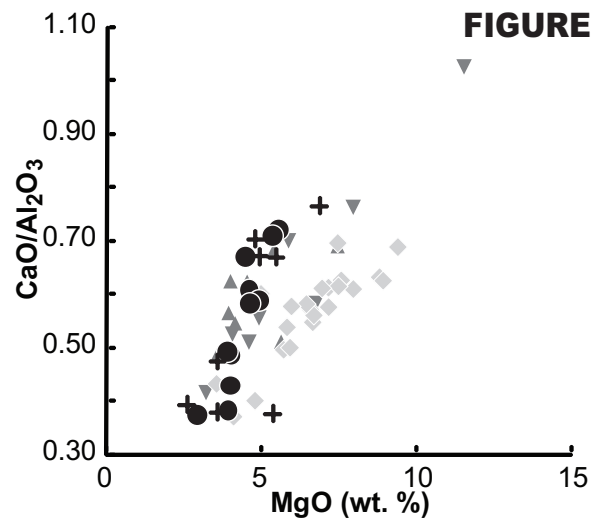
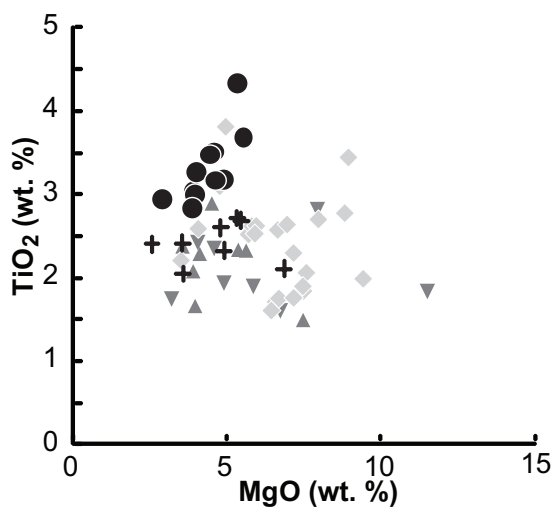


FIGURE 4C

- ▼ Guguftu
- ▲ Choke
- ◆ Getra Kele
- + Group 4b (25-22 Ma)
- Group 4a (20-12 Ma)

Figure 5a

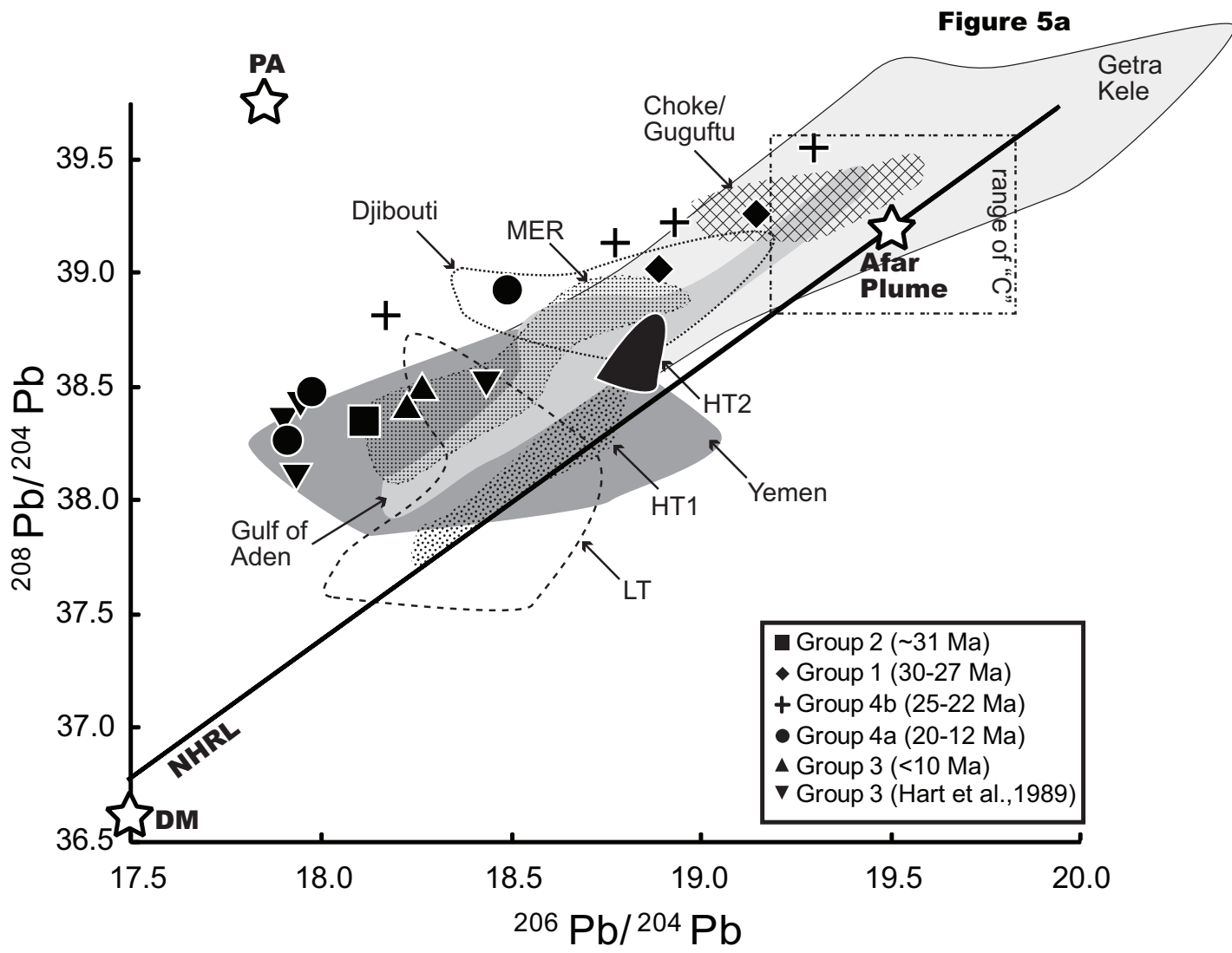


Figure 5b

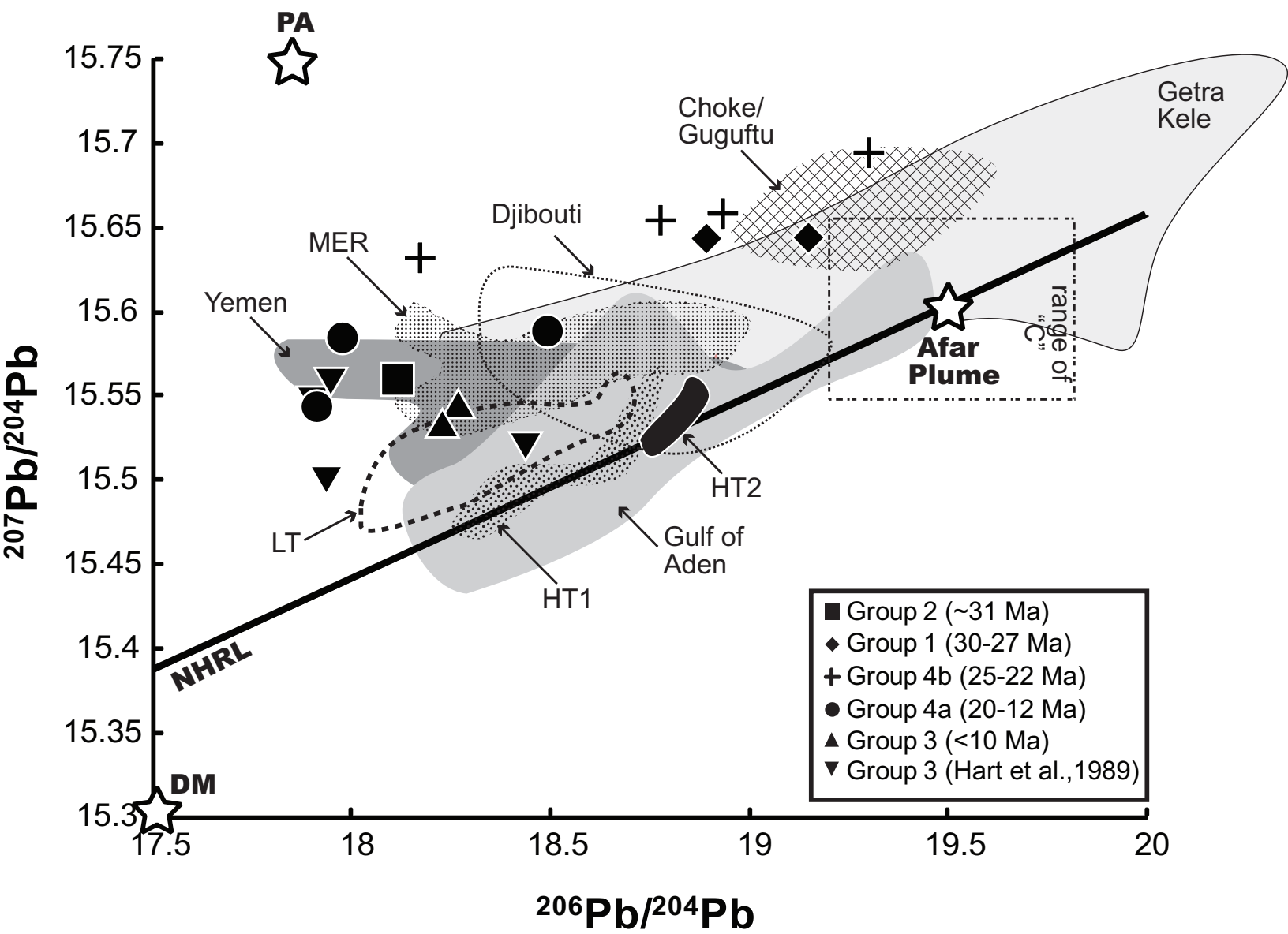




Figure 6

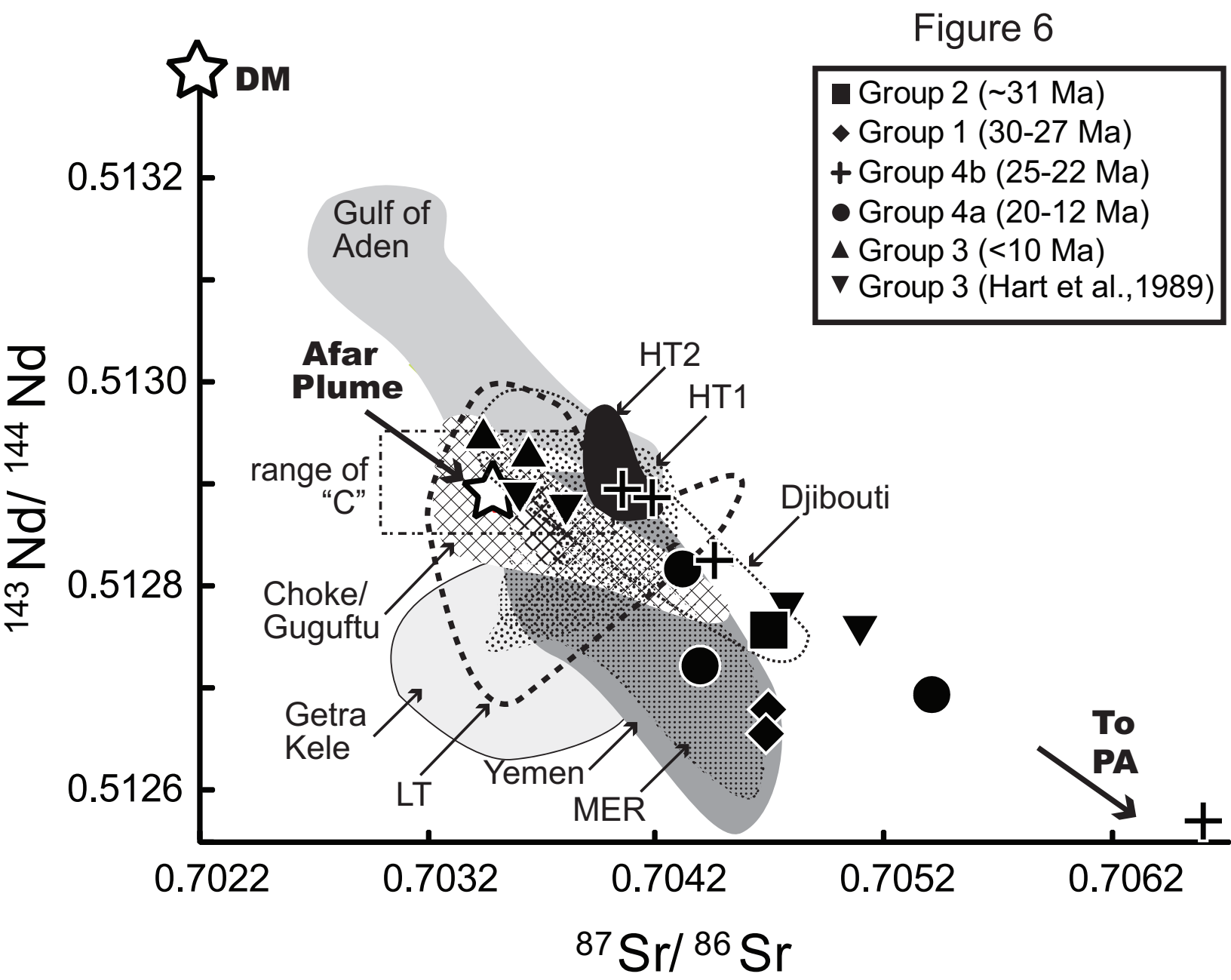


Figure 7

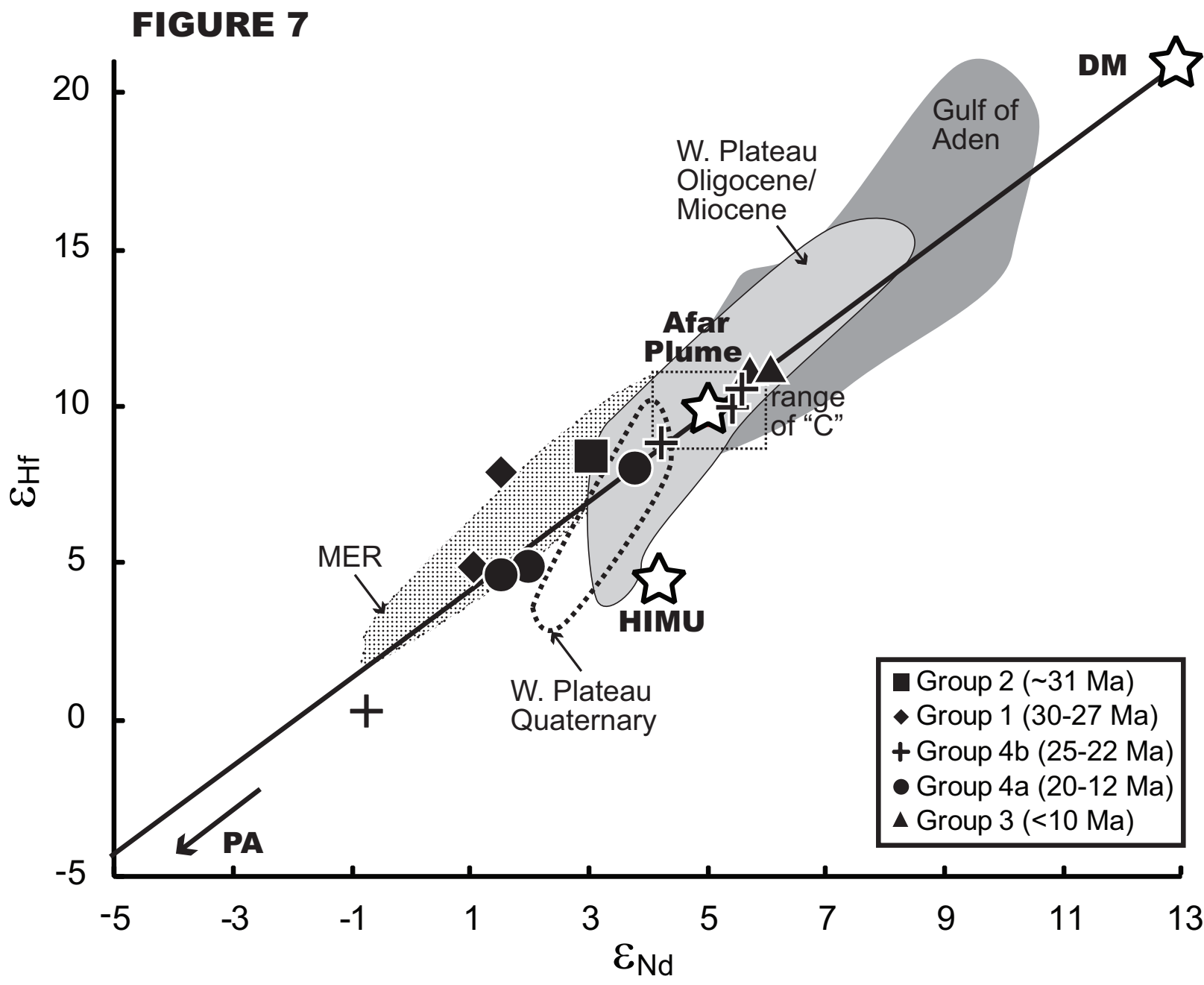


Figure 8

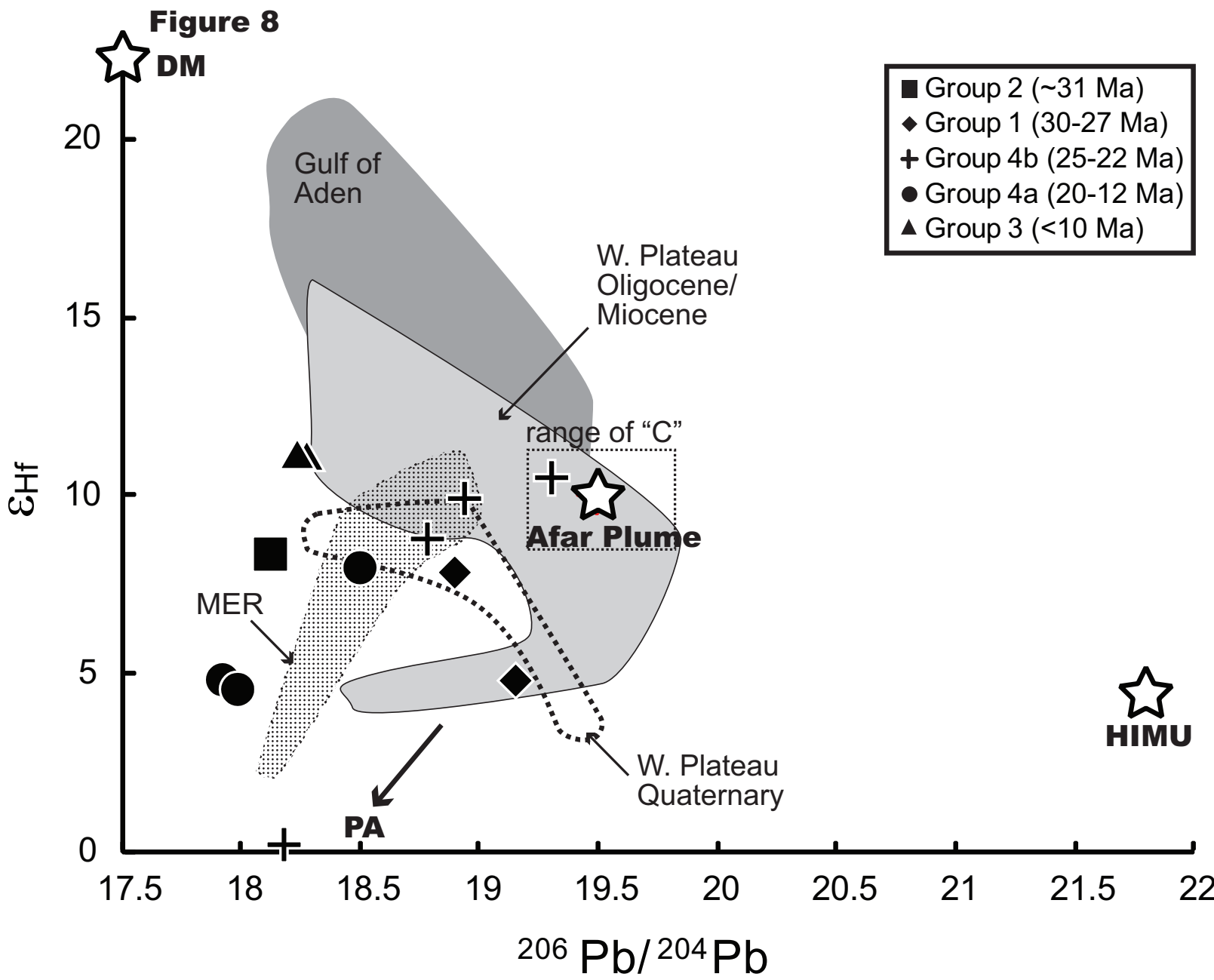


Figure 9

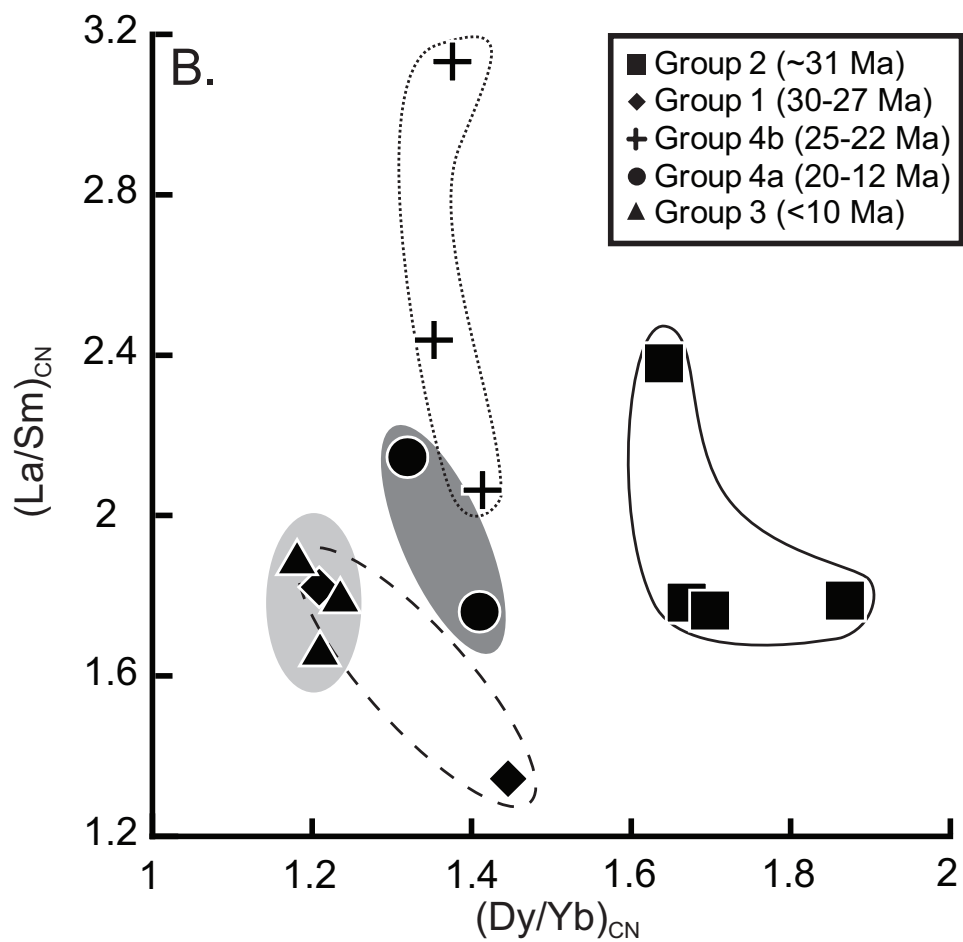
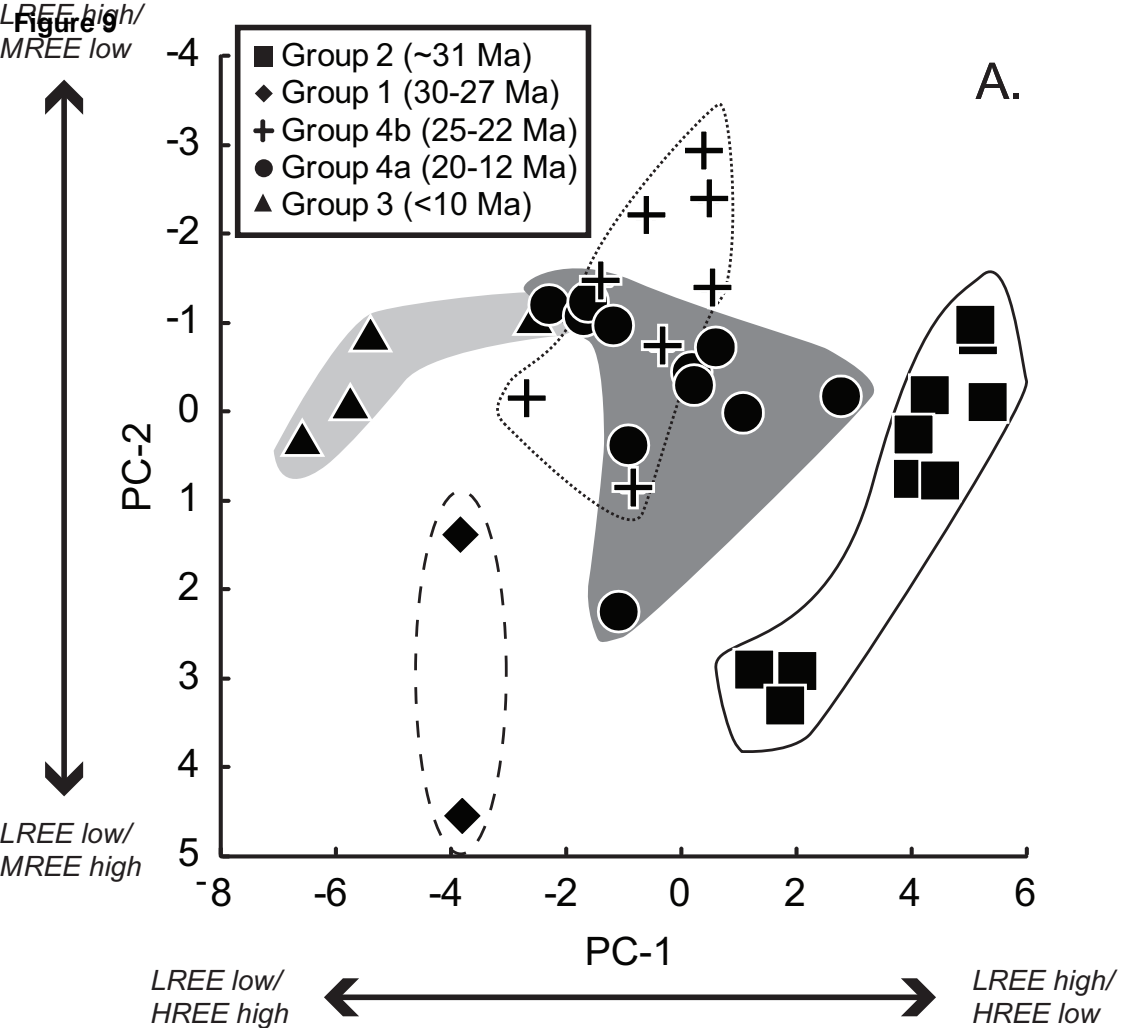
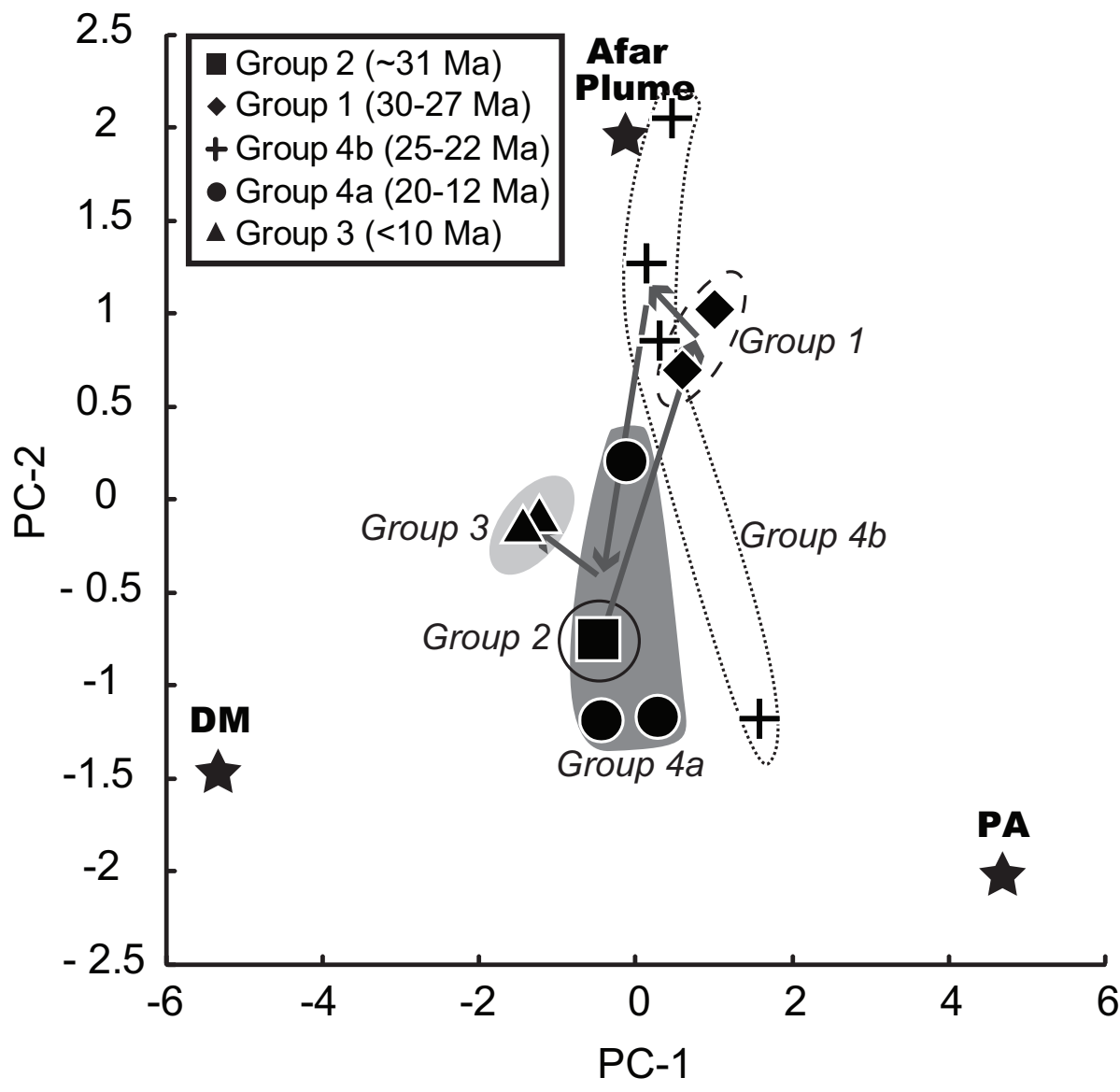


Figure 10



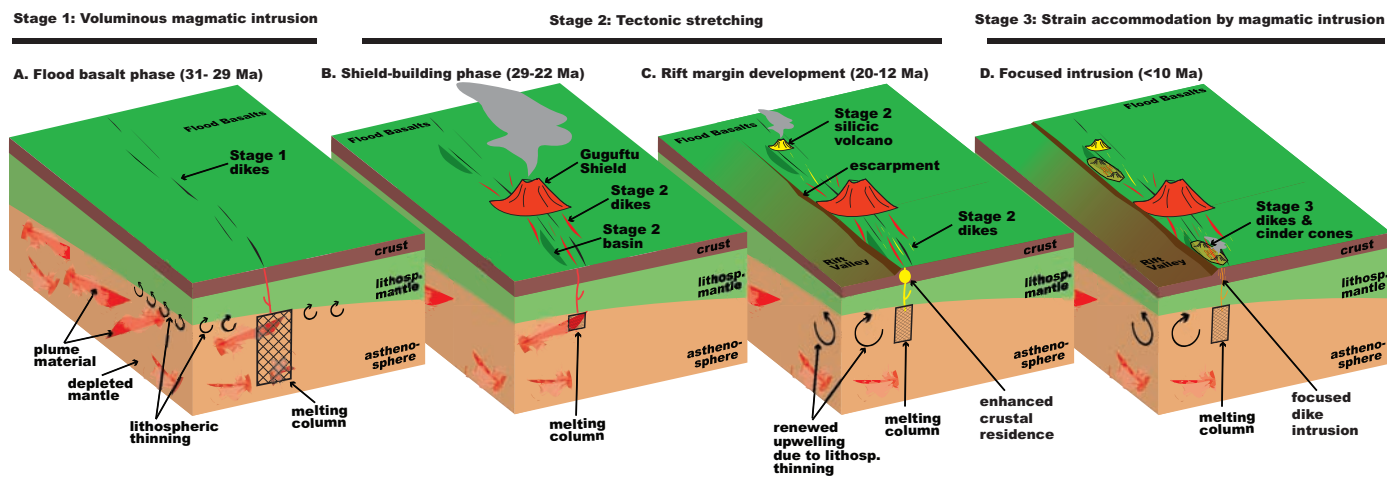


Figure 11